The Thesis Committee for Naif Mohammed Alrubaie
Certifies that this is the approved version of the following thesis:

Dynamic Petrophysical Properties of Laminated Rocks: An Experimental Investigation

APPROVED BY
SUPERVISING COMMITTEE:

Supervisor:

Carlos Torres-Verdín

Co-Supervisor:

Zoya Heidari

Dynamic Petrophysical Properties of Laminated Rocks: An Experimental Investigation

by

Naif Mohammed Alrubaie

Thesis

Presented to the Faculty of the Graduate School of

The University of Texas at Austin

in Partial Fulfillment

of the Requirements

for the Degree of

Master of Science in Engineering

The University of Texas at Austin

December 2018

Dedication

To my family.

Acknowledgements

I would like to express my gratitude and appreciation to my supervisor, Dr. Carlos Torres-Verdín, first for giving me the opportunity to join his group, and second for providing me with support and guidance throughout my graduate program. I also thank my co-supervisor, Dr. Zoya Heidari, for her support and guidance in this research. Special thanks go to Dr. Kishore Mohanty and Dr. Nicolas Espinoza.

I thank everyone in my research group, namely, Dr. David Medellin, Dr. Roger Terzian, Dr. Joaquin Ambia-Garrido, and Mr. Reynaldo Casanova. Also, I thank Mr. Glen Baum, Mr. Gary Miscoe, Mr. Jith Liyanage, Mr. Daryl Nygaard, and Dr. Krishna Panthi; I learned a lot from them. I thank my fellow graduate students whom I met and interacted with on both a professional and a personal level; I wish you all a successful future.

Last but not least, I express my appreciation to the management of Saudi Aramco for sponsoring me to study at one of the best universities in the U.S. Special thanks go to Mr. Charles Bradford, my mentor, and to Mr. Nasreddine Hammou.

The work reported in this thesis was funded by The University of Texas at Austin Research Consortium on Formation Evaluation, jointly sponsored by AkerBP, Anadarko, Aramco, Baker-Hughes, BHP Billiton, BP, China Oilfield Services LTD., Chevron, ConocoPhillips, DEA, ENI, Equinor ASA, Halliburton, Inpex, Lundin-Norway, Nexen, Petrobras, Repsol, Schlumberger, Shell, Southwestern, TOTAL, Wintershall and Woodside Petroleum Limited. X-ray microfocus scanning was performed at the Chevron Digital Petrophysics Laboratory overseen by Dr. Nicolas Espinoza.

Abstract

Dynamic Petrophysical Properties of Laminated Rocks: An Experimental Investigation

Naif Mohammed Alrubaie, M.S.E.

The University of Texas at Austin, 2018

Supervisor: Torres-Verdín, Carlos

Co-Supervisor: Heidari, Zoya

Laminae included in rock samples are small-scale heterogeneities that introduce anisotropy to the larger-scale rock system. They can be described in terms of grain size variations, as in a clastic sediment that is interbedded with shale layers. Such variations in grain size translate into variations in pore and pore-throat size distributions, and they control the effective two-phase fluid transport properties of the rock. Ultimately, they impact hydrocarbon recovery. This thesis implements an experimental workflow to study and quantify the impact of laminations on dynamic petrophysical properties in the presence of two distinct types of layering: cross and parallel. Accordingly, relative permeability and capillary pressure are measured under two flow conditions: across (perpendicular flow) and along layers (parallel flow).

Two cylindrical composite rock samples were fabricated in which the first composite sample was interbedded with a lower permeability rock (Berea sandstone interbedded with Kentucky sandstone), and the second one was interbedded with a higher

permeability rock (Kentucky sandstone interbedded with Berea sandstone) to represent the layering cases defined above. Multiple laboratory experiments were carried out to measure mercury intrusion capillary pressure (MICP) and saturation-dependent relative permeability. These measurements were complemented with micro-computed tomography images and nuclear magnetic resonance (NMR) measurements. For the perpendicular flow experiments, I sealed the sub-samples into a cylindrical sample in order to allow mercury to flow across them. The seal surrounds the samples and forces mercury to intrude only through the two ends (faces) of the composite samples. In the parallel flow experiments, I first sealed each piece individually and then sealed the entire stack. This was done to ensure that flow pathways between the pieces were sealed.

A bimodal pore-size distribution in the Berea interbedded with Kentucky and in the Kentucky interbedded with Berea samples was revealed by MICP measurements in the parallel layering composite cores. In the cross-layering experiments, I observed a bimodal pore-size distribution for the two rock arrangements. Relative permeability was higher in the parallel flow composite cores compared to the perpendicular flow composite cores.

In core data analysis, samples are taken from intervals considered representative of one single rock type. When the data are quality checked, petrophysical measurements from samples that exhibit grain laminations are often excluded. This bias propagates to simulation work and leads to results that often do not match field data.

Table of Contents

List of Tables

List of Figures

Chapter 1 – Introduction

In this chapter, I introduce some of the previous work that was published on the subject of small-scale heterogeneities and their effect on relative permeability and capillary pressure. Next I outline the approach used to investigate the variation in these two dynamic petrophysical properties experimentally, and I present the motivation behind the investigation. The objectives of this research are also presented at the end of this chapter.

1.1 Previous Research

The effect of laminations on dynamic petrophysical properties has been previously considered and investigated. Corey and Rathjens (1956) investigated analytically and experimentally the effect of stratification – as in laminated rocks – on relative permeability in an oil and gas system of two layers with different permeabilities and capillary pressures. The system was assumed in both parallel and series types of arrangement. Capillary pressure and relative permeability curves of an oil-gas system were calculated using the following equations:

$$\frac{1}{{P_c}^2} = C\, S_{oe} \ , \tag{1}$$

$$K_{ro} = {S_{oe}}^4 \ , \tag{2}$$

and

$$K_{rg} = (1 - S_{oe})^2\,(1 - {S_{oe}}^2)\,, \tag{3}$$

where P_c is capillary pressure, S_{oe} is effective oil saturation, C is a constant, that was assumed to be equal to 1 and 10 in the high- and low-permeability layers, respectively, and K_{ro} and K_{rg} are the relative permeability to oil and gas, respectively.

Experimentally, Berea sandstone was used to confirm the findings of the analytical solution. Relative permeability was measured in parallel and normal flowing conditions. These experiments were not replicating the actual assumptions of the analytical approach. Therefore, the results were used qualitatively. Building an experimental model with two different rocks was assumed to be "impractical" given that there would be a capillary (or flow) discontinuity between them. Corey and Rathjens (1956) concluded that (1) relative permeability was dependent on flow orientation in stratified geology because of capillarity differences, (2) parallel flow relative permeability was higher than normal flow relative permeability at any given saturation, and (3) tight rocks would act as flow barriers in the case of normal flow.

Capillary pressure differences in laminated clastic reservoirs were investigated numerically to examine capillary trapping in differently arranged heterogeneous settings (Corbett et al., 1992). In this study, capillary pressure and oil and water relative permeabilities were calculated using the following equations:

$$P_c = C\, S_e^{-1/\lambda} \sqrt{\frac{\Phi}{K}} \ , \tag{4}$$

$$K_{ro} = 0.85\ (1 - S_e)^3 \ , \tag{5}$$

$$K_{rw} = 0.3\ (S_e)^3 \ , \tag{6}$$

and

$$S_{wc} = 0.6 - 0.165 \log K \ , \tag{7}$$

where P_c is capillary pressure, C is a constant that includes interfacial tension, S_e is normalized saturation, λ is the pore-size distribution index (which was assumed to be 1.5 for all generated capillary pressure curves), ϕ is porosity, K is permeability, K_{ro} and K_{rw} are the oil and water relative permeabilities, respectively, and S_{wc} is connate water saturation.

Equation (7) relates permeability to connate water saturation, which was derived from field data, whereas residual oil saturation was fixed at 0.3 for all layers regardless of permeability. A model of alternating layers that have permeabilities of 500 and 50 mD (milli-Darcy) was used to simulate waterflood at capillary-dominated flow as opposed to viscous-dominated flow. The balance between these two forces (capillary and viscous forces) in waterflooding can be determined by the ratio of the two, as shown in equation (8). Hence, flow rate was the changing variable to study the influence of capillary forces in such a heterogeneous layered system.

$$\frac{Viscous\ Forces}{Capillary\ Forces} = \frac{q\ \Delta x\ \mu_o}{K_x\ \Delta y\ \Delta z\ dP_c/dS} \tag{8}$$

Figure 1-1 shows the performance of the waterflood for series and parallel models at different rates. It was concluded that, when the layers were modelled in series, oil was trapped in layers with high permeability (500 mD) because water blocked its flow via layers with low permeability (50 mD), assuming the system was water-wet. In contrast,

when the layers were modelled in parallel, oil was not trapped, but it was swept form the layers with low permeability into the layers with high permeability (Corbett et al., 1992).

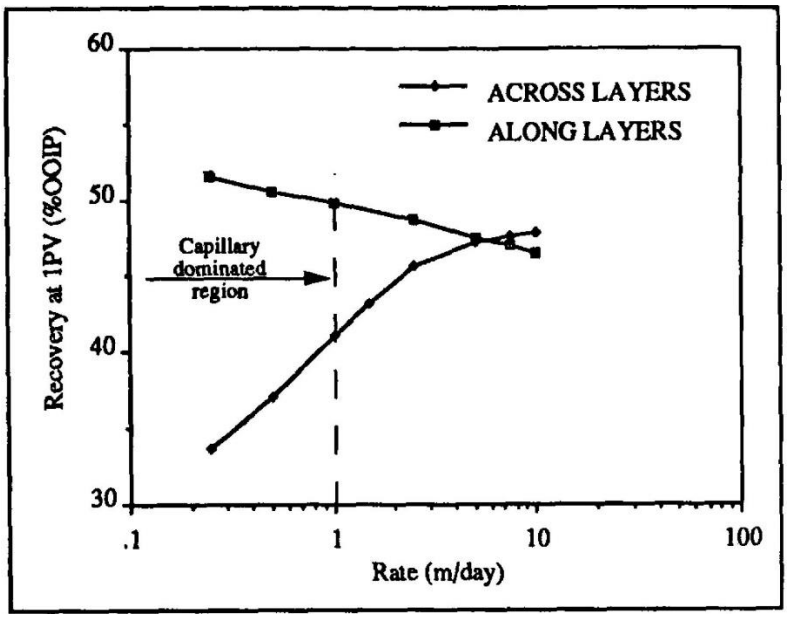

Figure 1-1: Recovery across layers and along layers simulated at different rates, emphasizing the capillary-dominated region (Corbett et al., 1992).

Honarpour et al. (1994) investigated the same problem experimentally on cores cut from a rock that exhibits parallel laminations to bedding planes. They measured oil and water relative permeabilities (drainage and imbibition) with cores drilled parallel and perpendicular to the laminations. Drainage and imbibition capillary pressures were also measured on cores drilled parallel and perpendicular to the laminations. It was concluded that relative permeability had directional characteristics, and therefore, a unidirectional relative permeability was not a correct representation of the effective flow characteristics of laminated rocks. Effective oil and water permeabilities were higher in the cores drilled parallel to than the cores drilled perpendicular to the laminations. Significant relative

permeability hystereses were observed in the laminated cores; however, the hysteresis was more pronounced in the cores drilled parallel to laminations. Capillary pressure was measured using the centrifuge method, and during the drainage cycle, there were no significant differences in the capillary pressure curves at any given saturation, but the cores drilled parallel had higher irreducible water saturation than the ones drilled perpendicular to the laminations.

In another related numerical and experimental study, the effectiveness of upscaling both relative permeability and capillary pressure of laminated sandstone reservoirs without accounting for their heterogeneity and anisotropic nature was investigated (Honarpour et al., 1995). This work showed that water was capillary trapped in low-permeability laminae during drainage and that oil was capillary trapped in high-permeability laminae during imbibition. This matches the conclusions of previous studies. Also emphasized was that simulation models should be used to consider the geological heterogeneities of the rock and the directionality of both relative permeability and capillary pressure for an accurate and effective scale-up.

The geological types of heterogeneity and their geometry (architecture) in sandstone formations, i.e., cross, ripple, and planar laminations, were studied numerically and found to be a principal factor in interpreting relative permeability data; reservoir modelling and upscaling should carefully account for these different types of heterogeneities (Ringrose et al., 1996). An interesting point that was analyzed in this research was the influence of small-scale heterogeneity on the ratio of viscous to capillary forces (equation 8). Small-scale heterogeneity had a greater impact on capillary forces, while large-scale heterogeneity had a greater impact on viscous forces. This relationship was demonstrated by a cross-plot of the ratio of capillary to viscous forces versus the length scale of heterogeneities for different permeability contrasts between the system's

constituent layers (Figure 1-2). Lamination scale is in the range of millimeters to centimeters (0.001 to 0.01 m scale), and therefore, capillary forces were the dominant forces.

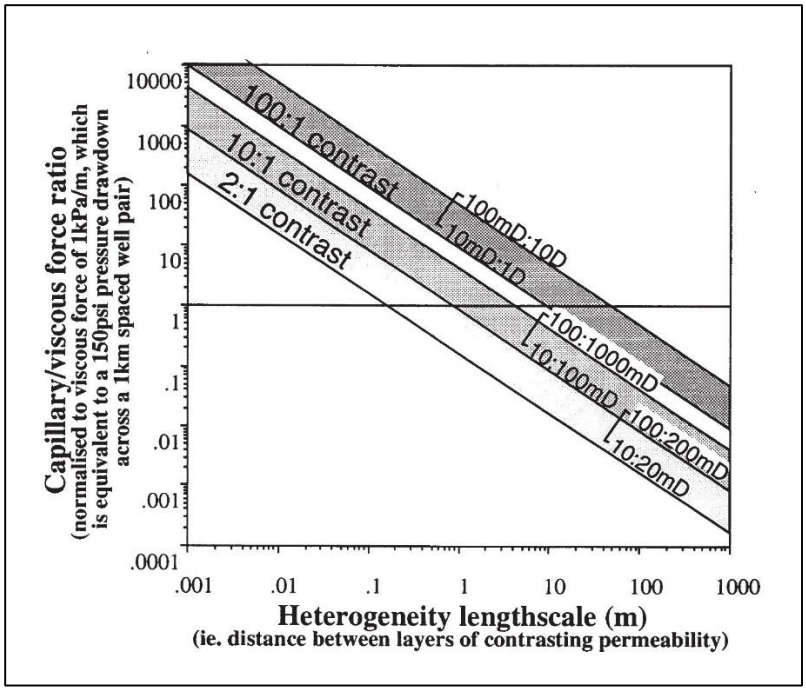

Figure 1-2: Ratio of capillary to viscous forces versus the length scale of heterogeneity for different permeability contrasts (Ringrose et al., 1996).

1.2 OUR CONTRIBUTION

This investigation examined the effect of laminations on relative permeability and capillary pressure, by fabricating two composite cores of three cylindrical core samples. The first had two high-permeability core samples and one low-permeability core sample in the middle; the second had two low-permeability core samples and one high-permeability core sample in the middle. The composite cores were fabricated in two different layering

arrangements: the core samples were stacked side by side, representing a 90-degree cross layering scheme, and cut and stacked above each other, representing a parallel layering scheme. Therefore, the fluid flow properties were studied in parallel and perpendicular conditions. Figures 1-3 and 1-4 represent the fabricated composite cores. In the parallel layering arrangement, the samples were sealed separately and then as a whole. In the 90-degree cross layering arrangement, the samples were separated by very porous and permeable sponge to ensure that there was no flow discontinuity and to provide a cushion at the sample faces.

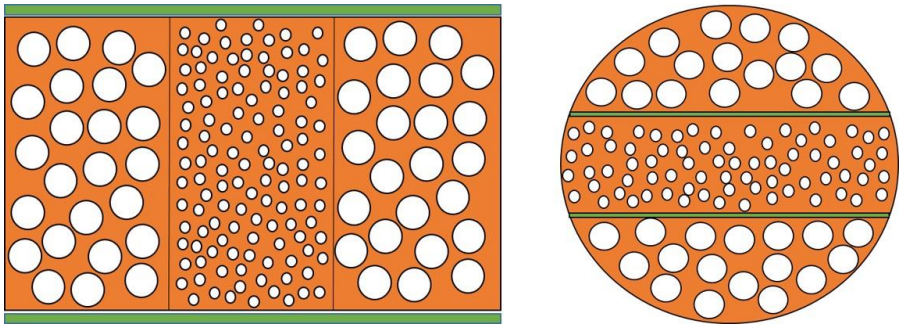

Figure 1-3: Representation of the two composite cores where the middle sample (the lamina) has a lower permeability than the two other samples; the composite core (left) represents 90-degree cross-layering, whereas the composite core (right) represents parallel layering.

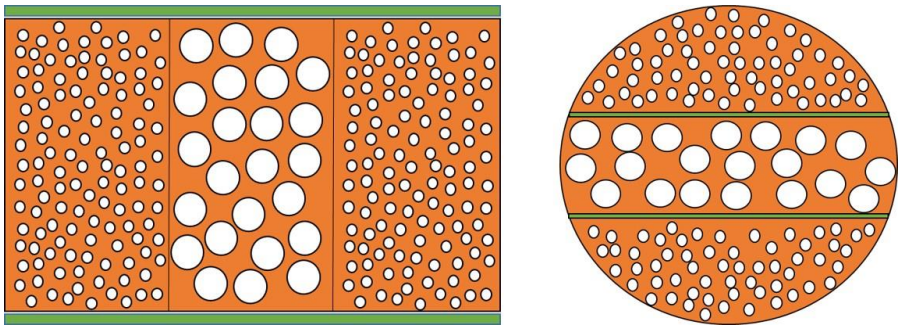

Figure 1-4: A representation of the two composite cores where the middle sample (the lamina) has a higher permeability than the two other samples; the composite core (left) represents 90-degree cross-layering, whereas the composite core (right) represents parallel layering.

I opted to conduct further complementary experiments on each sample: micro-CT images and NMR T_2 distributions were collected to help determine the matrix and pore structures. I wanted to realize the heterogeneity of the samples beforehand, and thus to select identical ones for the final composite cores. My intention was to replicate the geological nature of laminated sandstone formations in simple experimental models, which were used to investigate dynamic petrophysical properties.

1.3 Motivations and Objectives

The reason for pursuing this research is to find a solution to the problem of modelling and upscaling clastic reservoirs consisting of small-scale heterogeneities (laminations) in terms of their effective and equivalent dynamic petrophysical properties. Quantifying the effective fluid flow properties of laminated sandstone reservoirs is a challenge to reservoir engineers as well as petrophysicists. In this thesis, I approach a solution through a series of experiments to quantify how dynamic petrophysical properties change when fluids travel through such complex systems. Results of this study will provide insight and valuable data that can aid in constructing equivalent effective models of clastic

laminated reservoirs; the data will be used to further this research and quantify the impact of laminations on hydrocarbon production.

Figure 1-5 (Scholle, 1999) shows a laminated sandstone formation from an outcrop in West Texas. The laminations are within the millimeter to centimeter scale, and beds are within the centimeter to meter scale. This type of laminated systems should not be modeled using the petrophysical properties of the sand beds alone, but should be combined with an equivalent model that contains the effective petrophysical properties of the overall system.

Figure 1-5: Laminated sandstones in the Cherry Canyon Formation; for scale the knife is approximately 8 cm long (Scholle, 1999).

The objectives of this research are listed as follows:

- Investigate the effects of laminations on dynamic petrophysical properties, i.e., capillary pressure and relative permeability, using simple experimental models

- Examine both normal and parallel flow properties in composite cores
- Quantify the changes in the individual dynamic properties of the samples when combined into composite cores.

Chapter 2 – Methods

In this chapter, I explain the methods used in this research, starting with rock and fluid selections, then the materials and equipment used, and finally the workflow that was proposed and implemented.

2.1 Rock and Fluid Selections

To achieve the research objectives, two different sandstone rocks, Berea and Kentucky, were selected The difference in permeability between the two rocks is approximately three orders of magnitude. Berea has a high permeability, in the range of 150 to 350 mD, and Kentucky has a low permeability, in the range of 0.1 to 1 mD. This makes the two sandstone rocks perfect candidates for this study. The fact that both rocks are clastic would likely eliminate the possibility of having complex porous structures, Carbonate rocks, for instance, would most likely have complex porous systems. I considered using Cordova Cream (also called Texas Cream) limestone, which has a permeability range of 4 to 10 mD; however, one of the samples that was cut from a 30-cm-long core yielded a bi-modal results compared to results from another sample, and eventually was not used (Figure 2-1).

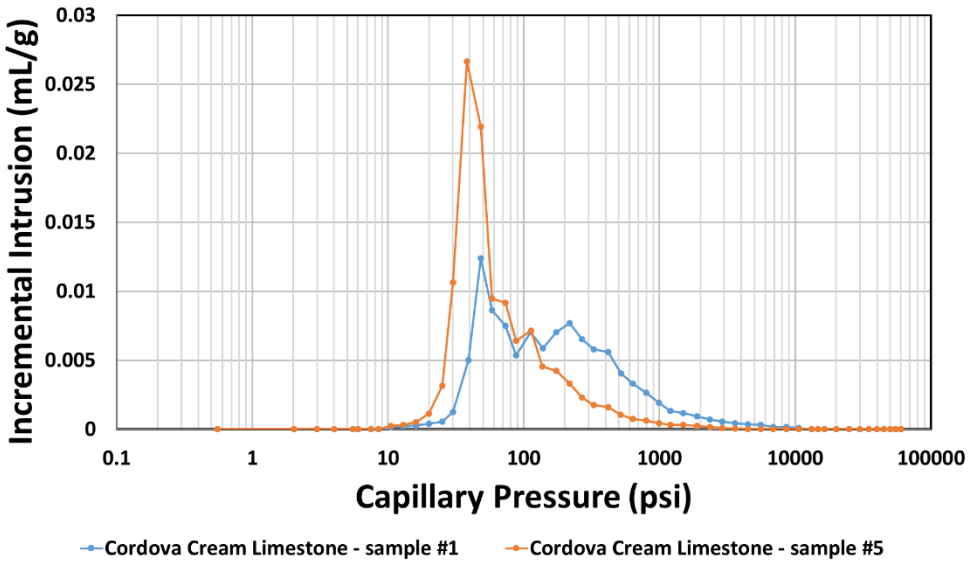

Figure 2-1: Incremental intrusion for two Cordova Cream limestone core samples that were cut from a 30-cm-long core. Sample 1 exhibits bi-modal pore-throat-size distribution compared to sample 5.

Berea sandstone has an average of 4 to 8 wt% (weight/weight percent) of clay minerals, which is considered as a low clay content sandstone rock, where the dominant constituents are kaolinite and illite (Mahmoud et al., 2015). These two clay types are not the worst type of clays that can make up sandstone rocks, e.g., smectite (Lake et al., 2014). In general, Berea is a rock that has been used extensively in research because of its nearly homogeneous nature as well as its superior petrophysical properties. It has been referred to as a "model" rock in the literature. On the other hand, the Kentucky sandstone has an average of approximately 14 wt% of clay minerlas, where the dominant constituents are illite (Mahmoud et al., 2015).

As for the fluid selection, a major factor was the rock-fluid interaction that could take place during the experiments; consequently, a 5 wt% NaCl brine (water) as the first (primary) fluid phase was used, and n-decane (oil) was used as the second fluid phase. The

salinity of the brine used is high enough (approximately 50,000 ppm) not to cause any clay activation in the sandstone cores. These fluids are commonly used in core flooding experiments, and thus their physical properties at different temperatures and pressures are reported in the literature.

2.1.1 Berea and Kentucky Sandstone

Table 2-1 shows the average petrophysical properties of Berea and Kentucky sandstone rocks (Mahmoud et al., 2015; "Sandstone Cores at Kocurek Industries," n.d.). These properties (except clay content) were assessed experimentally and the data are presented in Chapter 3.

	Berea	Kentucky
Average Porosity (%)	20	14
Average Permeability (mD)	100 – 300	0.1 – 1
Average Clay Content (%)	4 – 8	14

Table 2-1: Average properties of Berea and Kentucky sandstone (Mahmoud et al., 2015; "Sandstone Cores at Kocurek Industries.," n.d.).

2.1.2 Brine – 5 wt% NaCl Solution

Concentration of the NaCl brine used is 5 wt%. In other concentration units, namely, molality (moles of solute/mass of solvent), molarity (moles of solute/liter of solution), and parts per million (mass of solute/mass of solution multiplied by one million),

the concentration is approximately 0.9 molal or mol/kg, 0.883 molar or mol/L, and 50,000 ppm, respectively.

The density and viscosity of the 5 wt% NaCl brine are shown in Table 2-2. These values are extracted from tables that were available in the literature ("Density of Sodium Chloride Solutions," n.d.; Kestin et al., 1981; Ozbek et al., 1977).

Density (g/cc)	Viscosity (cP)
1.032	0.965

Table 2-2: Properties of 5 wt% NaCl Brine at 25 °C and 1 bar ("Density of Sodium Chloride Solutions," n.d.; Kestin et al., 1981; Ozbek et al., 1977).

2.1.3 n-Decane ($C_{10}H_{22}$)

The density and viscosity of the n-decane are shown in Table 2-3. These values are extracted from tables in the literature ("Decane," n.d.).

Density (g/cc)	Viscosity (cP)
0.725	0.838

Table 2-3: Properties of n-Decane at 25 °C and 1 bar ("Decane," n.d.).

2.2 MATERIALS

2.2.1 Heat Shrink Tubes

Heat shrink wrap tubes of two different sizes (1.5 and 1 inch) were used to wrap and seal the composite core samples for core flooding and MICP measurements. These shrink tubes were provided by Geophysical Supply Company. I used them in different cases as a wrap and seal; the first, when I fabricated the parallel flow composite system for relative permeability measurements, and the second, when I fabricated the perpendicular flow composite system for MICP measurements. These shrink tubes were found to wrap tightly around the core samples when exposed to a heat source (a laboratory oven or heat gun).

I tested the mercury intrusion into a sample of the heat shrink tubes used in our research. I intended to confirm that the heat shrink tube will not fail with high pressure mercury injection (Figure 2-2). The intrusion into the shrink tube only happens later (above 10,000 psi) after the intrusion of mercury into Berea and Kentucky sandstone cores, making it efficient for this project. Compression effects are observed between 1,000 and 10,000 psi.

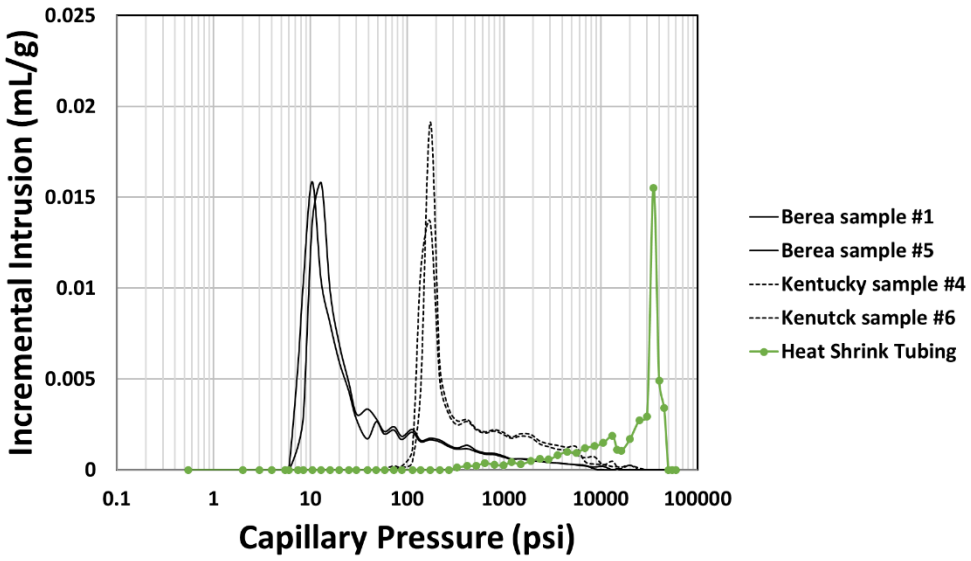

Figure 2-2: Mercury incremental intrusion data collected from two Berea and Kentucky core samples, and a sample of the heat shrink tubes used in this research. The shrink tube fails when the mercury injection pressure exceeds 10,000 psi.

2.2.2 Epoxy

Epoxy was used to coat and seal the samples prior to performing MICP experiments. Controlling the intrusion of mercury to mimic the specified flow condition was crucial, whether it is parallel or normal to the bedding plane. The epoxy used was EP30QF for high-performance bonding, sealing, and coating manufactured by Master Bond Inc. It has a compressive strength up to 24,000 psi, which means that it will hold up under high-pressure mercury intrusion experiments. This particular type of epoxy was used in previous research to study and correct for conformance and compression in MICP data of shale core samples, and it was found to work well under 40,000 psi of mercury injection pressure (Peng et al., 2017).

2.2.3 Sponges and Tissues

To provide flow continuity during core flooding of the composite cores, dishwashing sponges were cut to the shape and size of the core samples and inserted between the samples. Also, for MICP measurements, tissues were needed in between the samples for the same purpose. Sponges were used in between the samples in the composite systems; when brine flowed through the system, sponges were left in brine for a few hours, and when oil flowed through the system, sponges remained in oil for a few hours. Soaking the sponges was done to establish a wettability in favor of the injected fluid.

2.3 EQUIPMENT

2.3.1 Micro-CT X-Ray Imaging

Figure 2-3 shows the equipment used for micro-CT imaging, the Nikon XT H 225. It was important to understand and visualize the internal structure of the core samples. The samples were sandstone and were cored and cut, and later cut to smaller sizes, meant developing induced fractures were a possibility. Such fractures would complicate and change the pore structure. Thus, every core sample was scanned after coring and cutting using the micro-CT scanner. I first scanned and imaged the samples used for core flooding, and then later scanned and imaged the samples used for MICP measurements. The resolution of the images that were obtained was approximately 30 micrometer (micron) for the 1.5-inch-diameter and 5-cm-long samples used to measure NMR T_2 distribution, permeability, and relative permeability. In contrast, the resolution was higher (14 microns) for the 2-cm-diameter and 8-mm-long samples used to measure MICP.

Figure 2-3: The Nikon XT H 225 micro-CT scan equipment and workstation[1].

2.3.2 NMR Rock Analyzer

A Magritek 2 MHz NMR Rock Core Analyzer was used to measure the T_2 distribution and NMR porosities of the core samples (Figure 2-4). The goal was to confirm the homogeneity of the samples and to exclude the outliers that differ in their petrophysical properties.

All the samples were saturated with 5 wt% NaCl brine using a vacuum pump. The T_2 distribution of the samples was measured to determine their porosities and pore-size distributions. The T_2 distribution was a representation of the pore-body-size distribution because the samples were fully saturated with brine.

[1] X-ray microfocus scanning was performed at the Chevron Digital Petrophysics Laboratory at The University of Texas at Austin <https://faculty.engr.utexas.edu/espinoza/espinoza/microct>.

The P54 probe was used to perform the NMR experiments. This probe has a sample size limitation in that the largest sample to be fitted inside must have a diameter of 2 inches and a length of 2.5 inches (roughly 6 cm long). Therefore, new samples were cut with a length of 3 cm instead of 5 cm to measure the T_2 distribution of the composite cores.

Figure 2-4: The Magritek 2 MHz NMR Rock Core Analyzer and workstation.

2.3.3 Vacuum Pump

A Duoseal 1402 vacuum pump manufactured by Welch was used to saturate our samples with brine. Samples were saturated with brine for 24 hours, to allow removal of all the air in the samples. The samples were laid in a plastic container that has a cap connected to the pump.

First, the pump vacuumed the container of air along with the samples for 2-3 hours. Next, the brine was pumped into the container and the pump was kept running to fully saturate the samples. Sealing grease was applied to ensure that the container would be fully closed and sealed; thus, no air entered the container during the operation of the pump. This was checked by observing the sides where the cap closed on the container. If air entered the container, extra grease was applied in that zone.

2.3.4 Core Flooding Setup

For measuring permeability and relative permeability, a core flooding setup was used. A line diagram of the apparatus is shown in Figure 2-5. The setup is composed of a pump, an accumulator, a core holder, a back pressure regulator, and a pressure transducer. The setup tube lines (manufactured by Sandvik Group) are made of stainless steel, and can withstand pressure up to 10,000 psi.

In terms of the dead volume of the core flooding system including the tube lines and the back pressure regulator, the calculated cumulative dead volume was approximately 8 ml. All core flooding experiments were done at a constant flow rate, and the pressure difference was measured between the inlet and the outlet of the core holder.

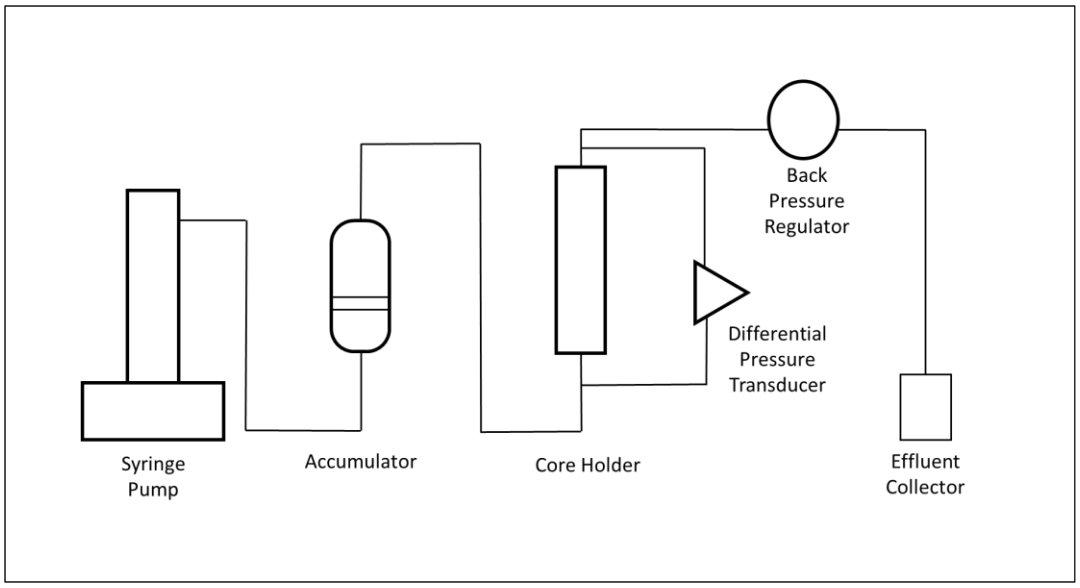

Figure 2-5: Line diagram of the core flooding setup, including (left to right) the pump, accumulator, core holder, pressure transducer, and back pressure regulator.

2.3.4.1 Pumps

I began the experiments using an older model pump: the ISCO LC-2600 Precision Pump, but later, I used a newer model, the Teledyne 500D Syringe Pump. The pump was filled with de-ionized water (DI water) as the pumping fluid. DI water was pumped into the accumulators, which in turn moved a piston that displaced the injection fluid into the core holder. Both pumps can operate at either constant pressure or constant flow rate; these experiments were carried out using a constant flow rate of core flooding. Both pumps were tested to ensure that the flow rate was accurate.

2.3.4.2 Accumulators

The accumulators used were made of stainless steel and could withstand pressure up to 3000 psi. The accumulator was composed of a piston that separates the pump and

injection fluid. The piston was moved by the pressure incurred by the pump fluid, hence displacing the injection fluid into the core holder. The capacity of the two accumulators was approximately 1 liter (500 ml each). Each accumulator held a different injection fluid; one accumulator was for injecting brine, and the other accumulator was for injecting oil (n-decane).

2.3.4.3 Core Holder

A Phoenix Instruments stainless steel, 1.5- by 12-inch core holder was used in the core flooding experiments. This core holder was limited to cylindrical samples that had a diameter and length of 1.5 and 12 inches, respectively. The core holder can hold pressure up to 10,000 psi, and it can withstand temperatures up to 300 °F (high pressure and temperature applications). It contains a sleeve that applied confining pressure on the core samples once it has been filled with a confining fluid (e.g., hydraulic oil). The core holder was mounted on a metal frame in the vertical position during core flooding. When water was injected into the core holder, the direction of fluid flow (direction of injection) was from the bottom to the top of the core holder, and vice versa when oil was injected into the core holder. Spacers were used to fill the remaining volumes inside the core holder because the core samples were 5 cm long.

2.3.4.4 Back Pressure Regulator

To regulate the pressure and flow rate during the core flooding experiments, a back-pressure regulator (dome-loaded back-pressure regulator), manufactured by Equilibar was used. The maximum pressure and temperature ratings of the back-pressure regulator are 6,000 psi and 150 °C, respectively. It is composed of a diaphragm that shuts the inlet and

outlet openings unless the incoming pressure is higher than the pressure applied against the diaphragm (Figure 2-6). The regulator was connected to the outlet of the core holder (to the downstream side). The dome-loaded back pressure regulator was pressurized to 400 psi using nitrogen gas delivered from a high-pressure gas cylinder, and it was kept constant at all times during core flooding experiments.

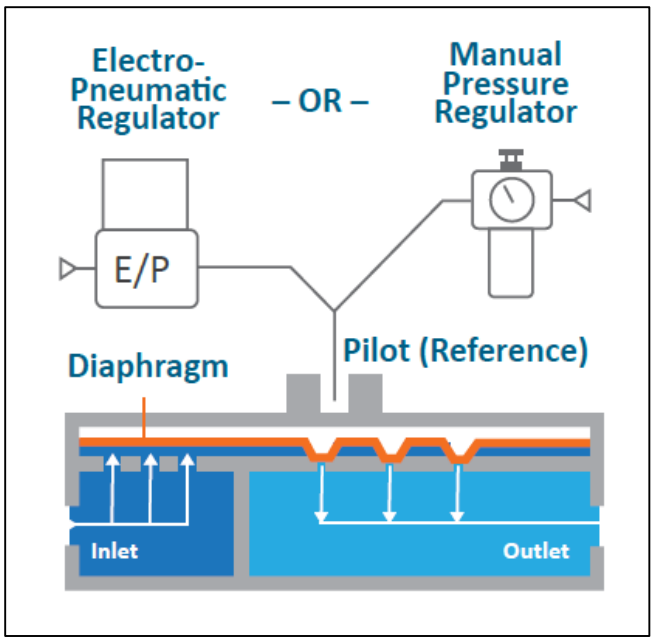

Figure 2-6: Internal structure of the Equilibar back-pressure regulator; the diaphragm (orange) controls (regulates) pressure and flow with reference to the loaded pressure ("Equilibar Research Series Back Pressure Regulators," n.d.).

2.3.4.5 Pressure Transducer

Differential pressure (between the upstream and downstream) data during the core flooding experiments were transmitted to a computer through a pressure transducer and a data acquisition card. The equipment used was a Rosemount differential pressure

transducer. It was limited to a maximum pressure drop of 300 psi between the high and low ports. Pressure data were viewed on the computer using LabView. Regular calibration of the pressure transducer was needed to ensure reliable data collection; calibration should be done monthly (Honarpour et al., 1986).

2.3.5 Mercury Porosimeter

A Micromeritics AutoPore IV 9500 porosimeter was used to perform mercury intrusion to measure the capillary pressure within the core samples. Samples were dried in an oven (temperature was set in the range of 70 to 90 °C) for over 24 hours prior to performing MICP measurements. Blank correction was applied on the cumulative intrusion data to account for mercury and glass compression during very high pressures. Capillary pressure (between mercury and mercury vapor) was measured up to 60,000 psi.

2.4 WORKFLOW

The Berea and Kentucky sandstone cores are cylindrical and were cored from outcrop rock blocks. They were cored to 1.5 inch in diameter and approximately 30 cm in length (Figure 2-7), and then cut into five equal samples, 5 cm each, for relative permeability measurements. This brings the total number of core samples to ten. Later, as the workflow progressed, I excluded a few samples and kept six core samples, three Berea and three Kentucky, for the composite cores. The composite core systems arranged in two flow configurations and were composed of two different fractions of Berea and Kentucky sandstone core samples (Figure 2-10). The Berea-Kentucky-Berea composite core is referred to as the BKB composite core, and the Kentucky-Berea-Kentucky composite core

is the KBK composite core. Figures 2-8 and 2-9 show the fabricated parallel BKB and KBK composite samples.

More core samples were later cut to replace some samples that had to be excluded, or to test some different fabrication techniques.

Figure 2-7: Berea (top) and Kentucky (bottom) core samples used for experiments. A 30-cm-paper ruler for scale.

Figure 2-8: A side view of the fabricated parallel composite samples, KBK (left) and BKB (right). These composite samples are 5-cm long.

Figure 2-9: A cross-sectional view of the parallel composite samples, KBK (left) and KBK (right). The diameter of these composite samples was approximately 1.5 in.

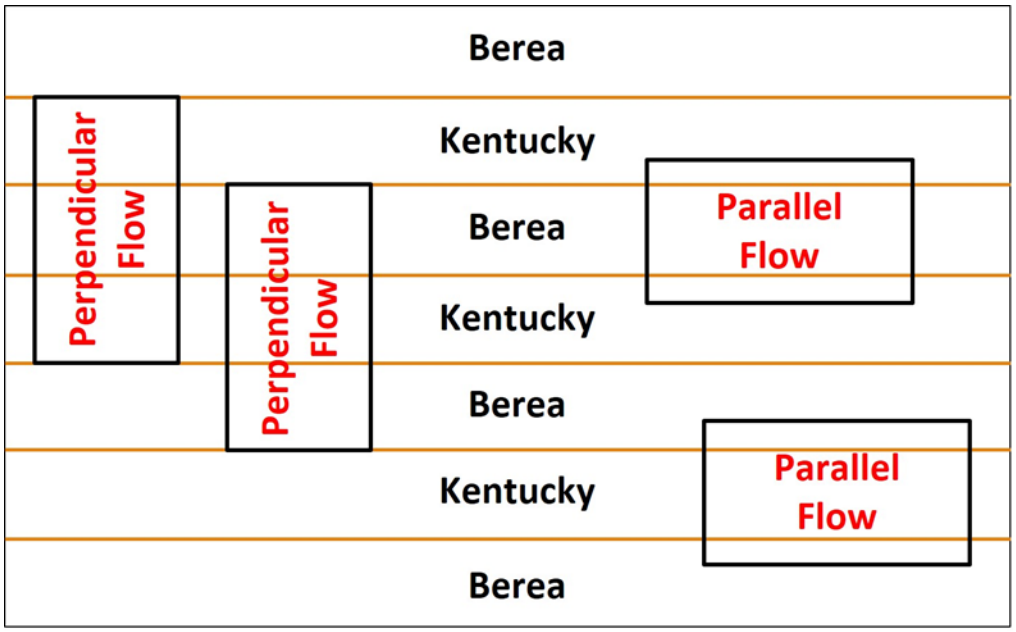

Figure 2-10: Composite core samples which were prepared for measuring flow properties in parallel and perpendicular flow conditions.

For capillary pressure measurements, the core samples were cut smaller than the original sample, down to 20 mm in diameter and 40 mm in length, and then cut into five equal samples, 8-mm-long each. Using six samples of each Berea and Kentucky sandstones, four composite core systems, BKB and KBK were created, to measure parallel flow (Figure 2-11) and perpendicular flow capillary pressure (Figure 2-12). The other samples that were not included in the composite systems were used to define the individual capillary pressure of Berea and Kentucky core samples. Because the samples were cut for capillary pressure measurements, they had to be imaged using the micro-CT scanner to confirm the absence of possible induced fractures.

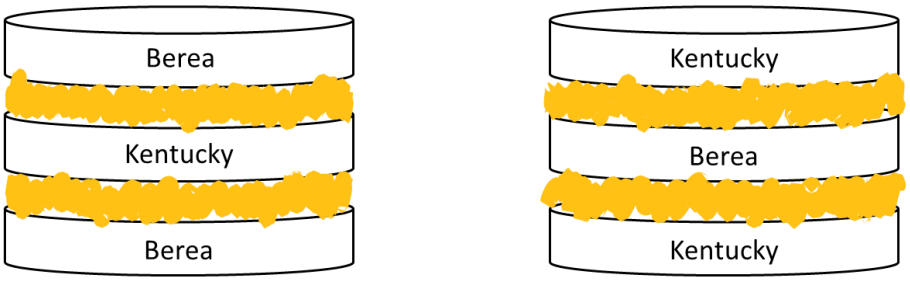

Figure 2-11: Samples separated with epoxy (yellow) to avoid mercury flow across the layers.

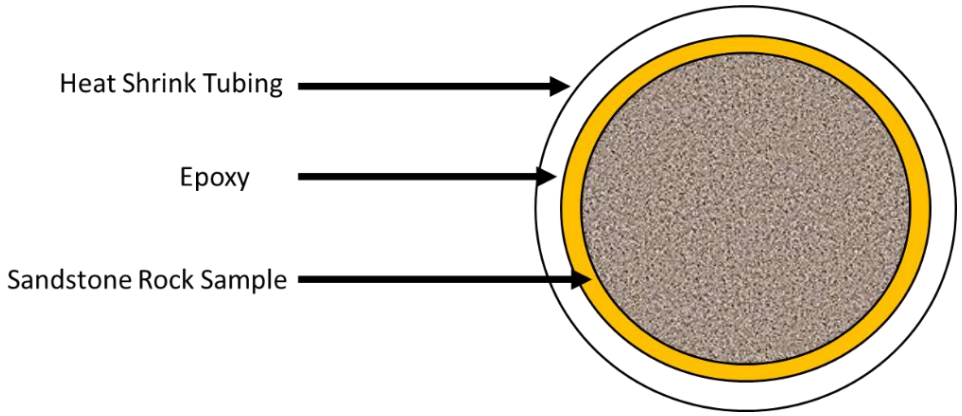

Figure 2-12: Samples were first coated with epoxy (yellow) and then sealed with heat shrink tube; hence, mercury would intrude across the samples.

The proposed and implemented experimental workflow is summarized as follows:

1. All ten samples were imaged using a micro-CT scanner to ensure that no induced fractures were present.
2. The ten samples were saturated with brine using the vacuum pump to ensure that they were fully saturated and that no air was trapped in the pores.
3. NMR T_2 distribution of all the ten samples was measured to determine their porosities and pore-size distributions.
4. The absolute permeability (brine as the base) of all ten samples was measured with the core flooding apparatus.
5. Three Berea and three Kentucky core samples were selected based on previously obtained data to fabricate the 90-degree cross layering composite system (cores stacked side by side).
6. The absolute permeability (brine as the base) of the BKB and KBK composite systems was measured.

7. Later, one Berea and one Kentucky core sample (not part of the composite systems) were core flooded with n-decane to determine their individual drainage relative permeabilities and irreducible water saturations (Sw_{irr}) using the unsteady-state method.
8. Then the drainage relative permeabilities and Sw_{irr} of the BKB and KBK composite systems were determined using the unsteady-state method.
9. One Berea and one Kentucky core sample were selected and then cut into three pieces along their axis in a defined measure (equal proportions).
10. Steps 1 and 2 were repeated.
11. All six pieces were sealed individually using heat shrink tubes and then every three were sealed together to fabricate the parallel layering composite systems (cores stacked on top of each other).
12. Steps 6 and 8 were repeated.
13. Two Berea and two Kentucky core samples were selected, and then cut into five equal 8 mm pieces (20 core samples in total) in preparation for capillary pressure measurements.
14. All 10 Berea and 10 Kentucky core samples were dried for more than 24 hours.
15. Step 1 was repeated.
16. Four Berea and four Kentucky core samples were selected (not part of the composite systems) to define their individual capillary pressure curves.
17. Three Berea and three Kentucky core samples were selected where the epoxy was applied on their perimeters (excluding the faces) and then they were sealed together with shrink tubes to fabricate the 90-degree cross layering BKB and KBK composite systems.

18. Capillary pressure of the perpendicular layering BKB and KBK composite systems was measured using MICP method.
19. The other three Berea and three Kentucky core samples were selected where the epoxy was applied one their faces (excluding the perimeters) to fabricate the parallel layering BKB and KBK composite systems.
20. Capillary pressure of the parallel layering BKB and KBK composite systems was measured using MICP method.

Chapter 3 – Results and Discussion

In this chapter, I present the results of the micro-CT images obtained, NMR T_2 porosities and distributions of Berea, Kentucky, and the BKB and KBK composite cores, and permeability and relative permeability measurements, as well as capillary pressure measurements of Berea, Kentucky, and BKB and KBK composite core systems, in both parallel and normal flow directions.

3.1 Micro-CT Images

Figures 3-1 and 3-2 show the images obtained for the Berea and Kentucky core samples. These images are from three different slices extracted from the top, middle, and bottom of each sample's total slices. These samples were 5 cm long and had a diameter of 1.5 inches. The effective pixel size was approximately 30 micrometers (micron).

In these images the core samples of both Berea and Kentucky are physically intact. The Berea core samples have larger grains compared to the Kentucky core samples, which causes different permeability values in these two rock samples.

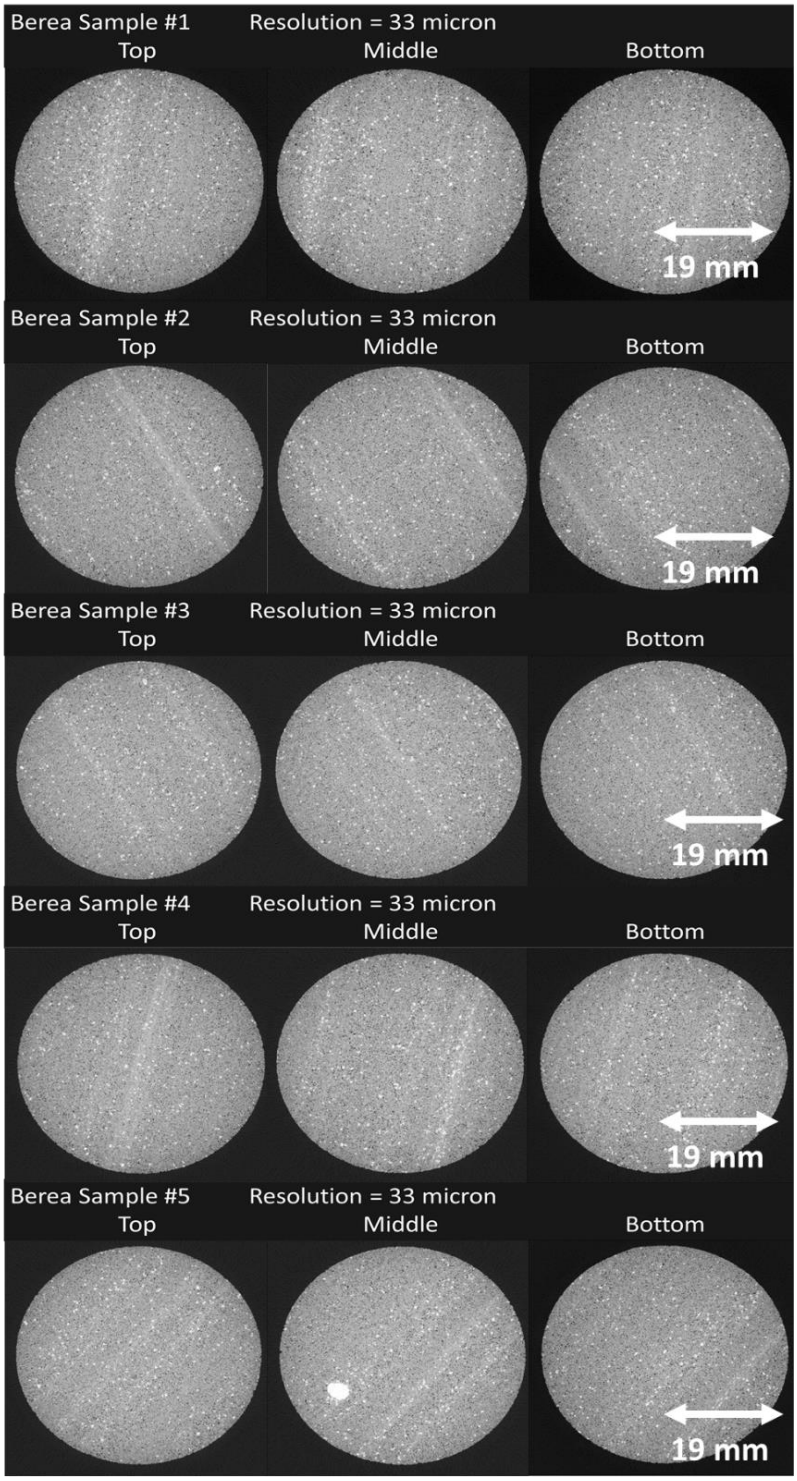

Figure 3-1: Micro-CT images of Berea sandstone for core samples 1 to 5. White double-sided arrow illustrates the scale.

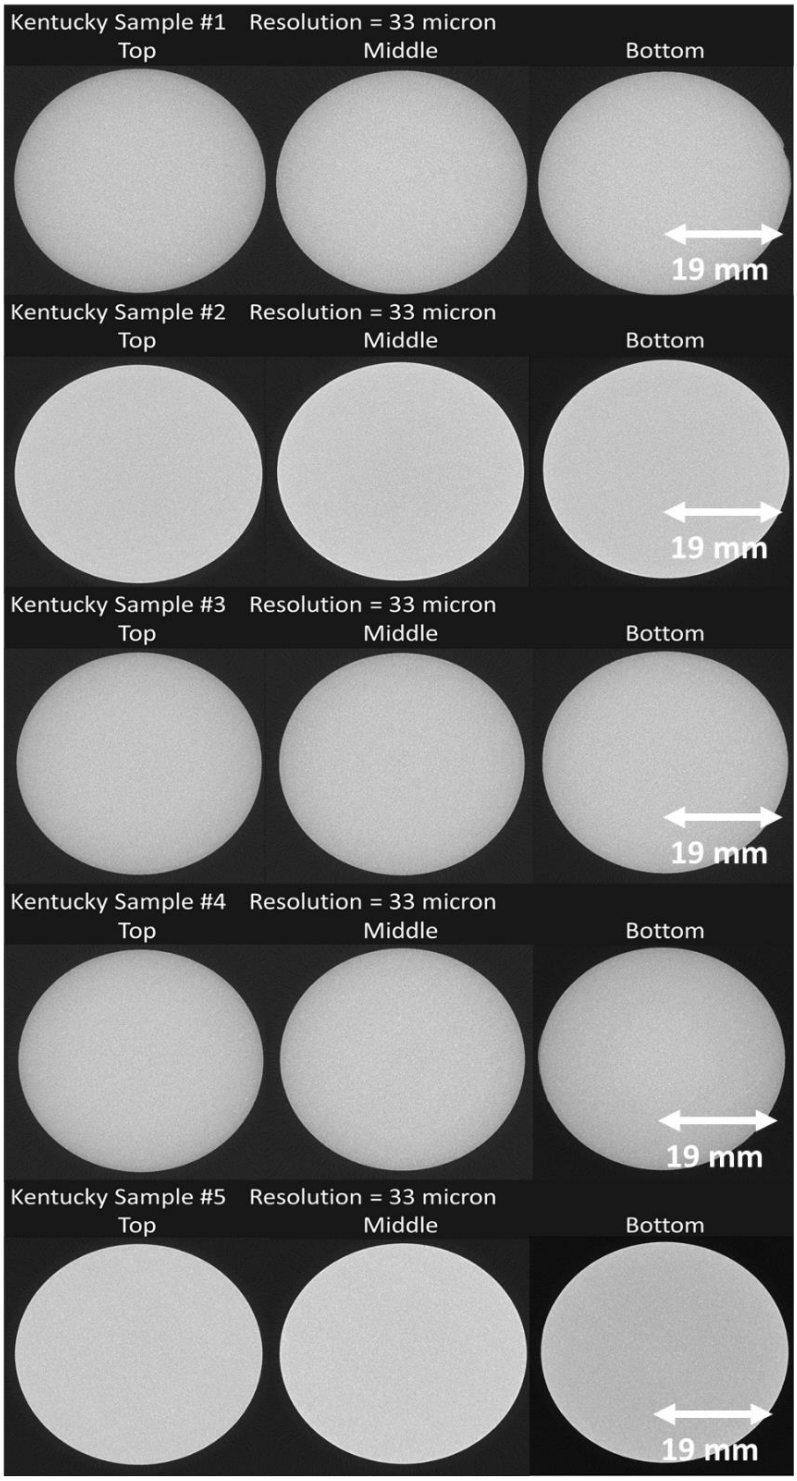

Figure 3-2: Micro-CT images of Kentucky sandstone for core samples 1 to 5. White double-sided arrow illustrates the scale.

3.2 NMR T_2 DISTRIBUTION

In preparation for NMR analysis, all core samples were 100% saturated with brine; thus, the T_2 distribution computed from the total magnetization would correlate to the pore-size distribution (pore-body distribution). T_2 is not directly measured but rather is calculated mathematically through an inversion process. Given the total magnetization, initial magnetization, and the time, T_2 distribution is determined using the following equation:

$$M(t) = \sum M_i(0)\, e^{-t/T_{2i}} \ , \tag{9}$$

where $M(t)$ is the measured magnetization at time t, $M_i(0)$ is the initial magnetization of the i_{th} component of relaxation, t is the time, and T_{2i} is the decay constant of the i_{th} component of transverse relaxation. The T_2 distribution represents the incremental porosity, and therefore the cumulative T_2 represents the total porosity (Dunn et al., 2002).

3.2.1 Berea Sandstone Core Samples

Figure 3-3 shows the T_2 distribution (incremental porosity) of eleven Berea sandstone core samples. The samples were homogeneous and they all had a similar T_2 peak location. Hence, the samples had similar pore-body distributions.

Figure 3-4 shows the cumulative porosity of the same eleven Berea sandstone samples. A small variation exists in the total NMR porosity of the eleven samples, because the samples were cut from different rock blocks of Berea sandstone. Samples 1 to 6 have almost the same NMR porosity (approximately 21%), whereas samples 7 to 10 and sample 14 have a slightly lower total NMR porosity (between 19 and 20%).

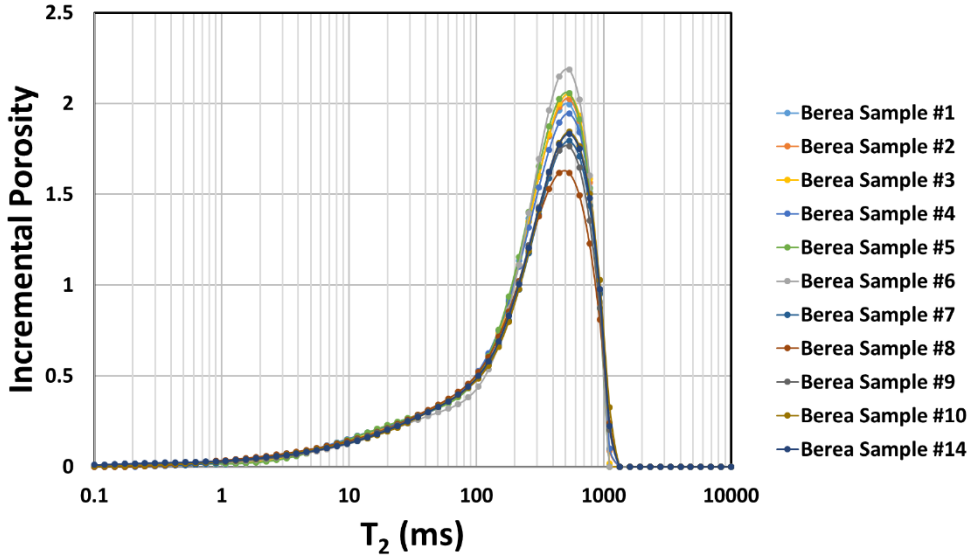

Figure 3-3: Incremental T_2 distribution of eleven Berea sandstone core samples.

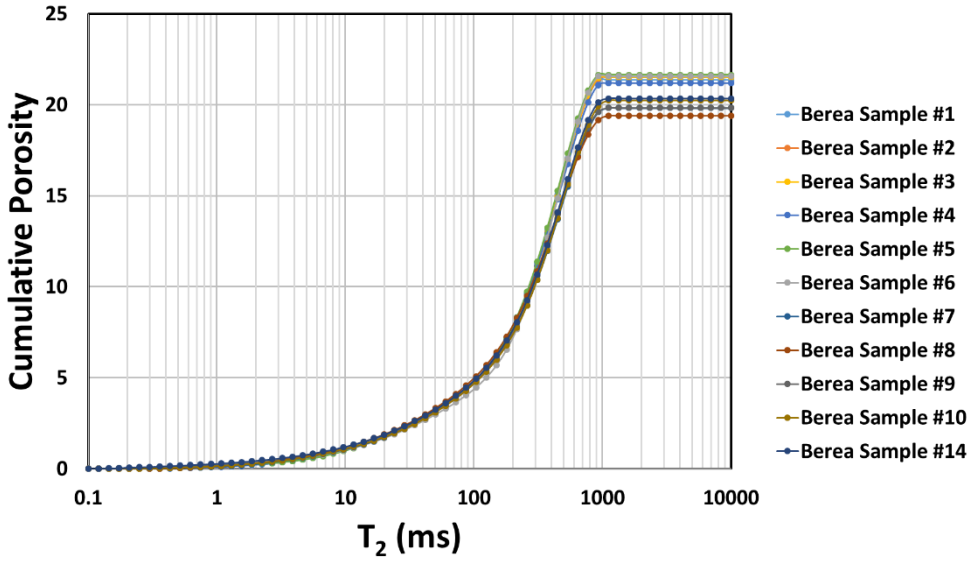

Figure 3-4: Cumulative T_2 distribution of eleven Berea sandstone core samples.

3.2.2 Kentucky Sandstone Core Samples

In contrast to the Berea samples, the Kentucky sandstone samples show variation in terms of their T_2 distribution (Figure 3-5). The Kentucky rock was not as homogeneous as the Berea, possibly due to the relatively higher clay content compared to Berea sandstone. This would indicate a slight variation in the pore-body distribution of the seven Kentucky core samples.

Figure 3-6 shows the NMR porosity of the seven Kentucky core samples. These core samples have almost the same porosity (between 14.5 and 14.9%).

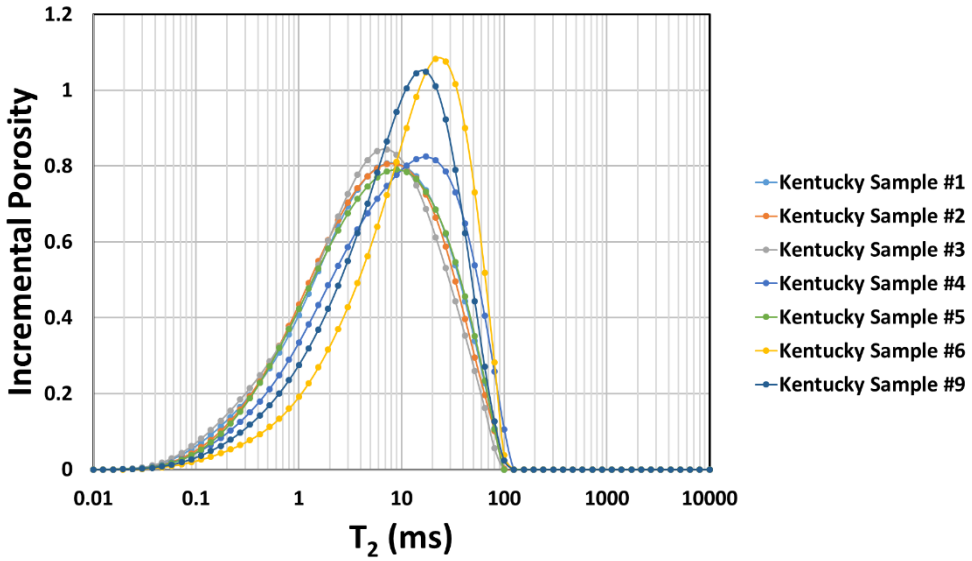

Figure 3-5: Incremental T_2 distribution of seven Kentucky sandstone core samples.

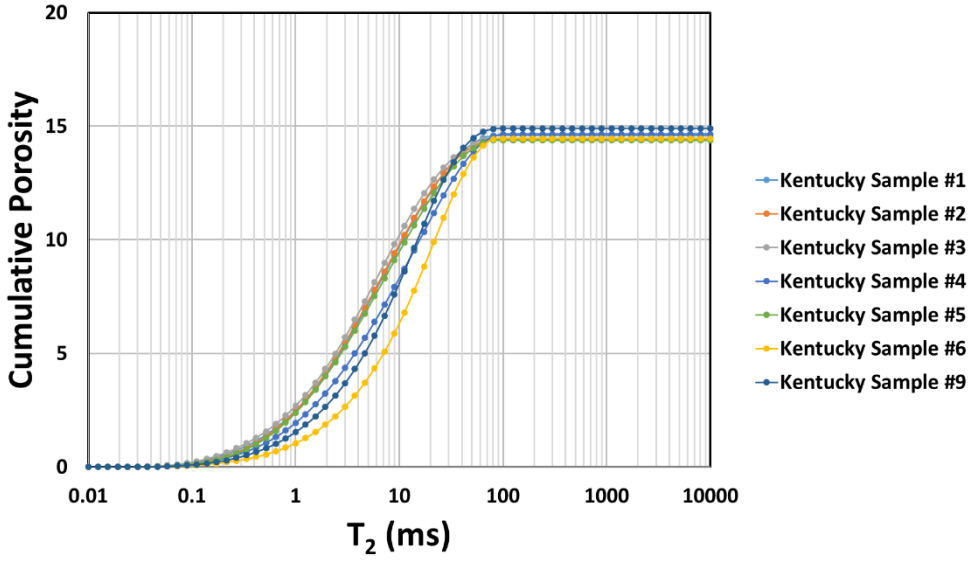

Figure 3-6: Cumulative T_2 distribution of seven Kentucky sandstone core samples.

3.2.3 Berea and Kentucky Composite Cores

To measure NMR porosity and T_2 distribution in the composite core systems, new samples had to be cut, because the NMR probe used in this research was limited to samples that were 6 cm long. Therefore, each Berea and Kentucky sandstone core samples were cut into 2-cm long. These core samples were cut from Berea core samples 11 and 12, and Kentucky core sample 7. The composite cores were made of Berea and Kentucky sandstone in different fractions (BKB and KBK), but were only arranged in series (Figure 3-7). The total length of the composite cores was 6 cm.

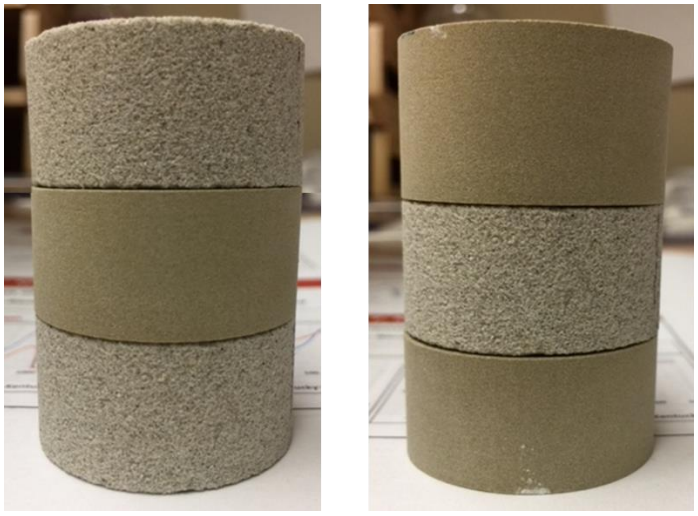

Figure 3-7: Composite cores, BKB (left) and KBK (right), that were used in measuring NMR porosity and T_2 distributions.

The individual T_2 values of Berea and Kentucky (Figure 3-8, 3-9, 3-10, and 3-11), were measured, as were the T_2 values of the BKB and KBK composite cores. The individual T_2 modes of Berea and Kentucky core samples combined in the two composite cores varied with the different fraction of each core (Figure 3-12).

The NMR porosities of the composite cores in turn represent also the different fractions of each Berea and Kentucky sample. The average porosity computed form the individual core samples yielded the same NMR porosity measured for the composite cores (Figure 3-13).

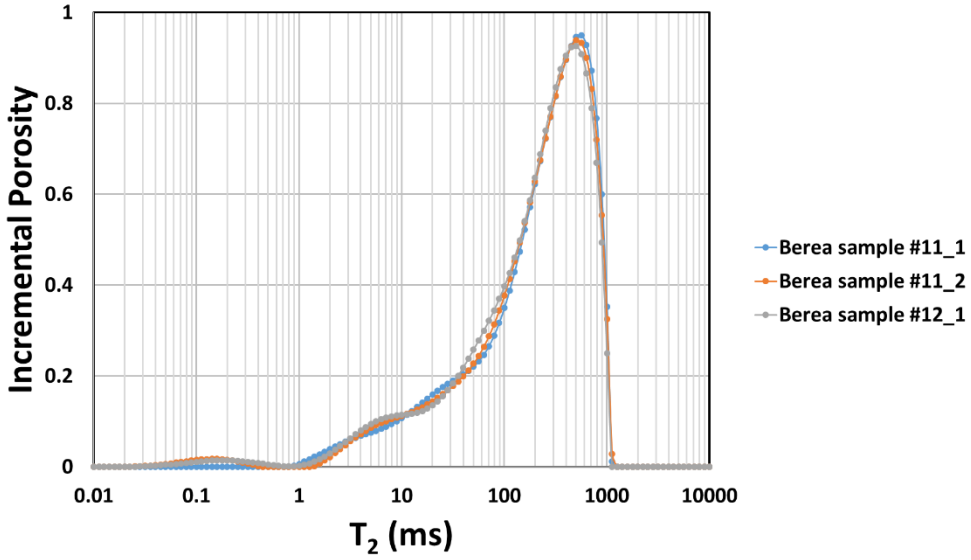

Figure 3-8: Incremental T_2 distribution of Berea core samples 11 and 12.

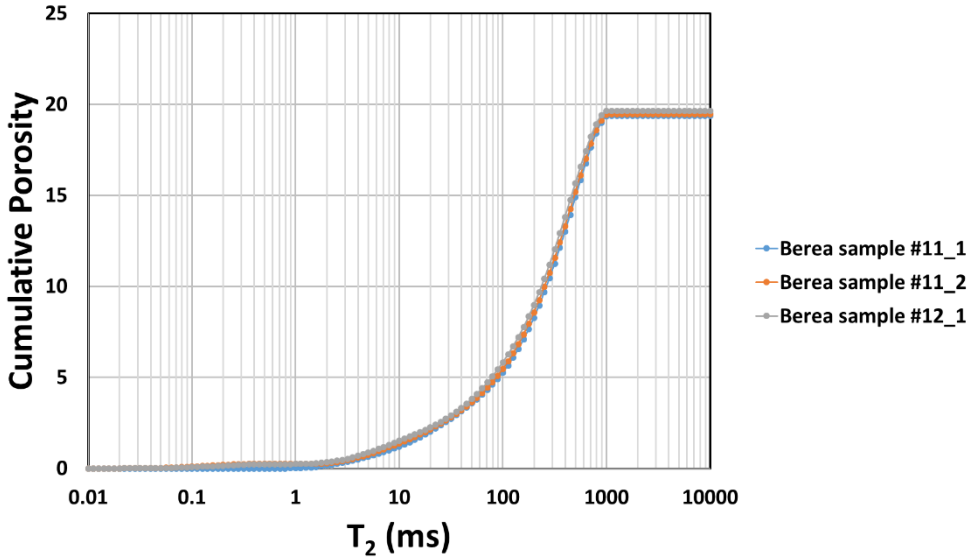

Figure 3-9: Cumulative T_2 distribution of Berea core samples 11 and 12.

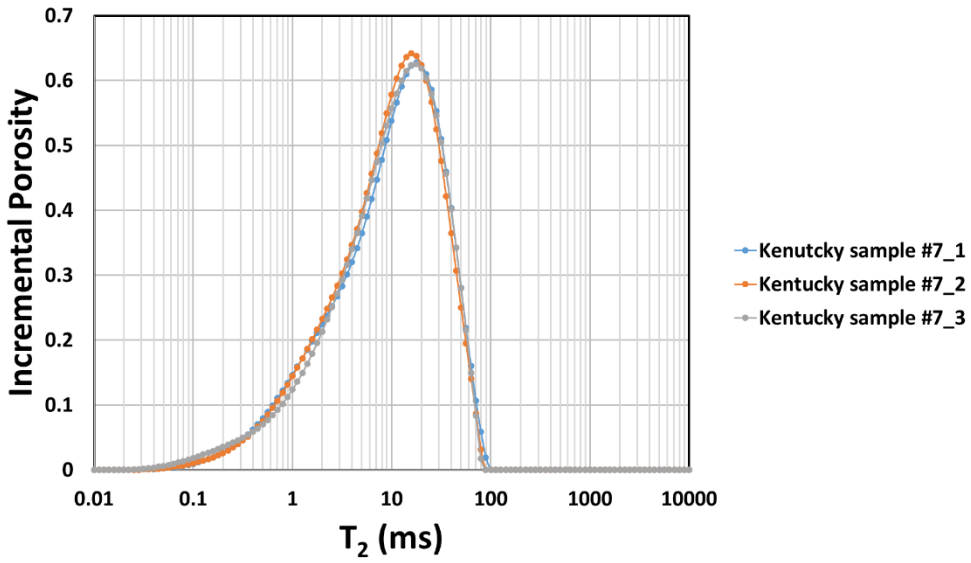

Figure 3-10: Incremental T_2 distribution of Kentucky core sample 7.

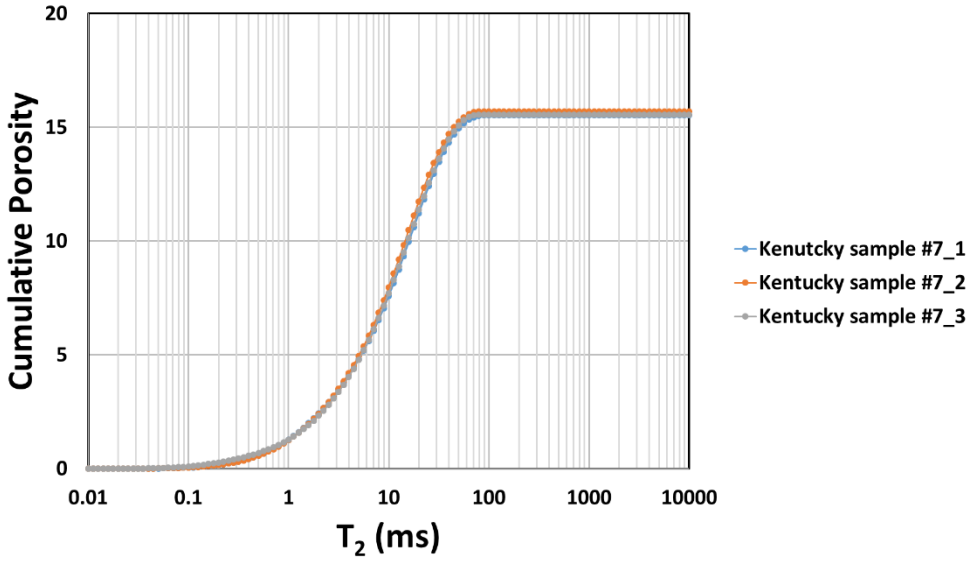

Figure 3-11: Cumulative T_2 distribution of Kentucky core sample 7.

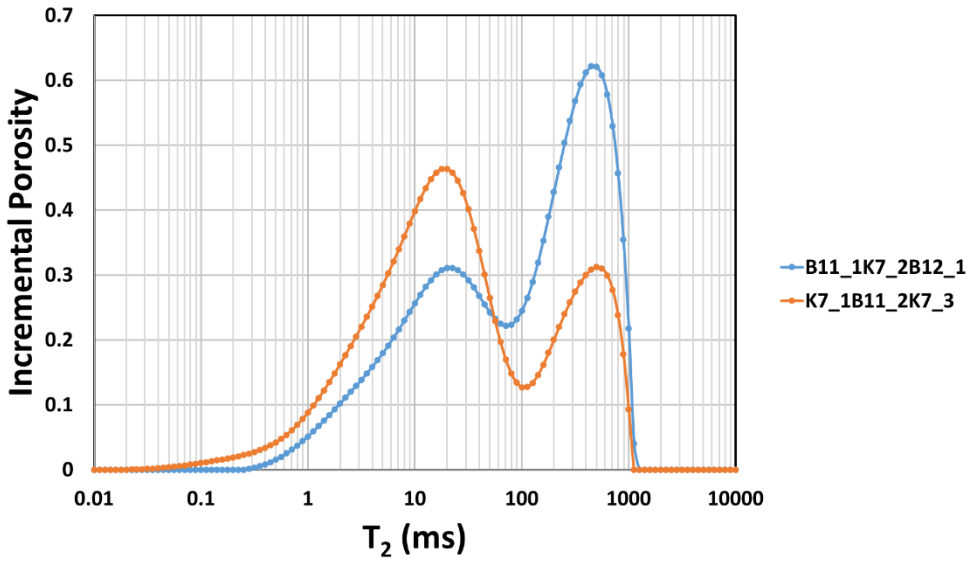

Figure 3-12: Incremental T_2 distribution of BKB (blue) and KBK (orange).

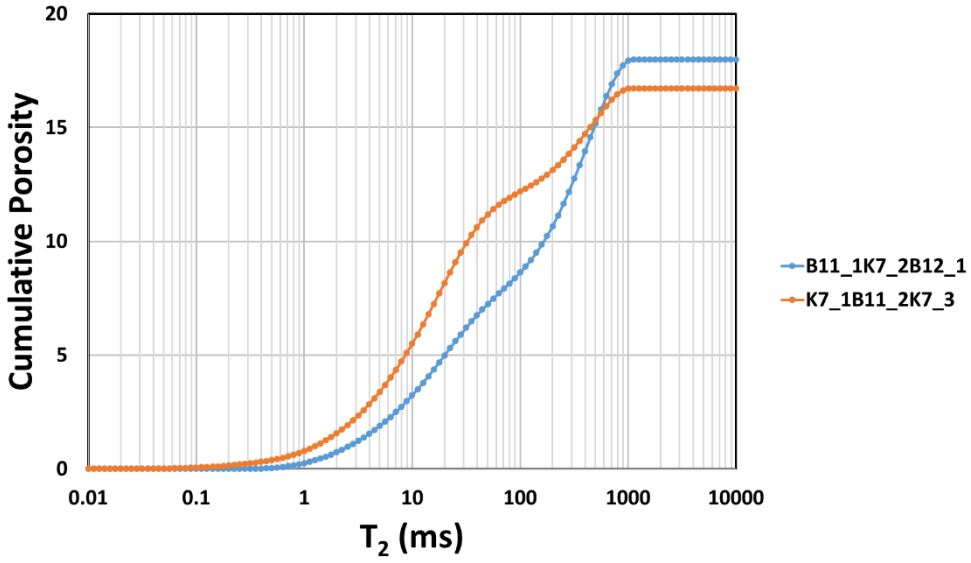

Figure 3-13: The cumulative T_2 distribution of BKB (blue) and KBK (orange).

3.3 ABSOLUTE PERMEABILITY

All the Berea and Kentucky core samples were flooded with brine, as a single phase, to determine their absolute permeabilities (brine permeability). The absolute or brine permeability of the Berea and Kentucky core samples was calculated using Darcy's law (Equation 10). The core flooding was performed at constant flow rate, and the pressure drop across the core samples was measured. Using the other parameters, the permeability of each sample (Peters, 2012a) can be calculated as

$$q = \frac{-K\,A\,\Delta P}{\mu\,L}\,, \tag{10}$$

where q is the flow rate through the core sample, K is the absolute permeability of the core sample, A is the cross-sectional area of the sample, ΔP is the pressure drop (differential pressure) across the sample, μ is the viscosity of the flowing fluid (injected through the sample), and L is the length of the sample.

The function that relates flow rate to differential pressure in Darcy's law (Equation 10) is linear. Therefore, the flow rate and differential pressure data from core flooding the core samples can be combined on a single plot for the purpose of better visualization.

In the case of Berea core samples, brine permeabilities were determined from multiple rates, given that it was easier and faster to flow brine through them than through the Kentucky core samples. Hence, Kentucky sandstone brine permeabilities were determined form a single rate test.

3.3.1 Berea Sandstone Core Samples

The following figure (Figure 3-14) shows injection rate as a function of differential pressure for multiple rate core flooding experiments of five Berea core samples. The slope of the data is similar, which correlates to the absolute permeability. Using that slope, the absolute permeability of these five Berea core samples is approximately 300 mD.

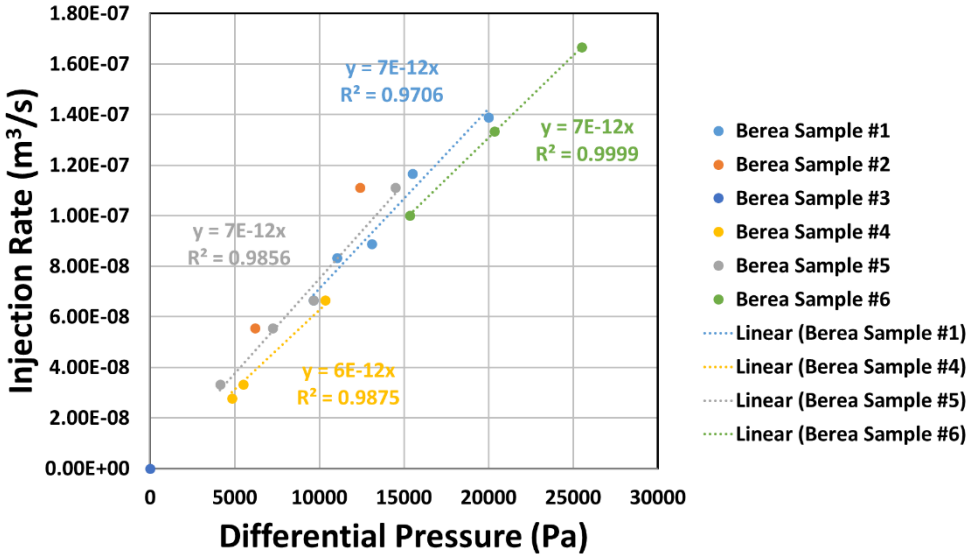

Figure 3-14: Collective data from multiple rate core flooding of five Berea core samples.

3.3.2 Kentucky Sandstone Core Samples

Figure 3-15 shows injection rate as a function of differential pressure from core flooding six Kentucky core samples. A slope cannot be drawn from these data, given that the core flooding experiments were not done in multiple rates but rather in one single rate. However, the aggregate of data indicates something about the proximity of the absolute permeability of the six Kentucky core samples, in the range of 0.16 to .024 mD.

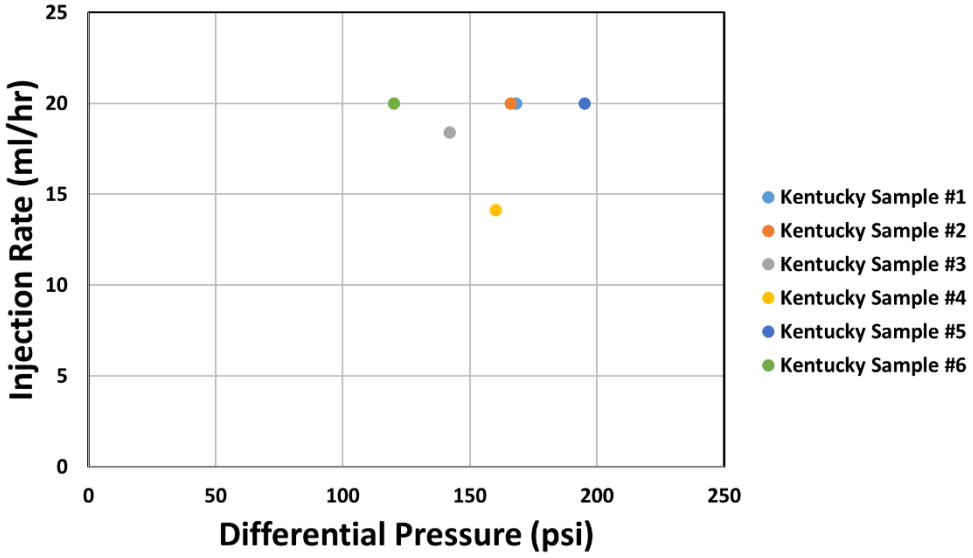

Figure 3-15: Aggregated data points from core flooding six Kentucky core samples. Calculated permeabilities of all samples are within 0.16 to 0.24 mD.

The next two cross-plots (Figures 3-16 and 3-17) show the differential pressure data collected during core flooding of Kentucky core sample 5. This core flooding was done at a single flow rate using the total capacity of the accumulator, 500 ml. The initial plan was to measure the differential pressure data until actual steady-state is reached, but that would need a larger accumulator (probably double the capacity of the one that was used), and the final differential pressure would not change the permeability of the Kentucky core samples significantly. After approximately 12 hours of core flooding, the differential pressure was approximately 191 psi, and 9 hours later, the differential pressure was approximately 195 psi. The difference in the calculated permeability is within 0.005 mD, and is considered insignificant.

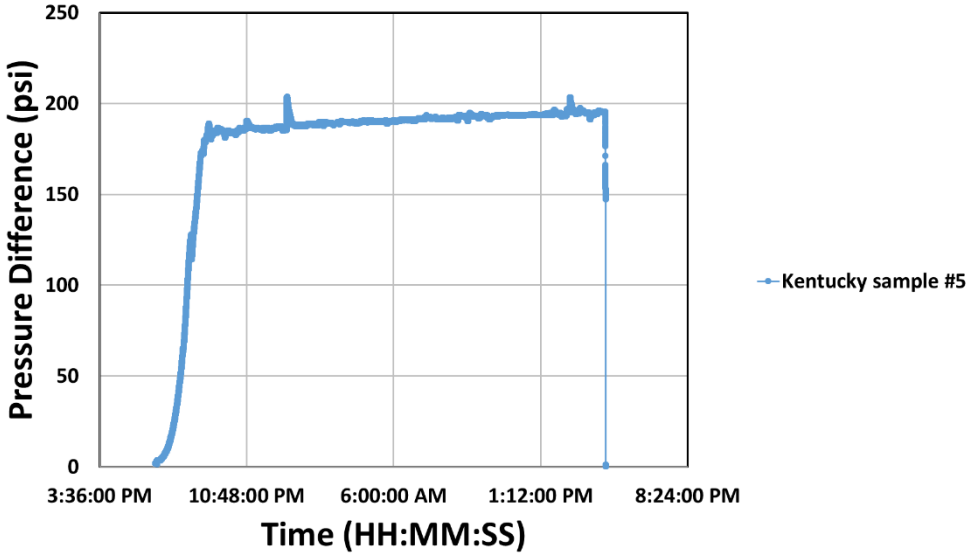

Figure 3-16: Differential pressure measured during the core flooding of Kentucky core sample 5, flooded for approximately 24 hr.

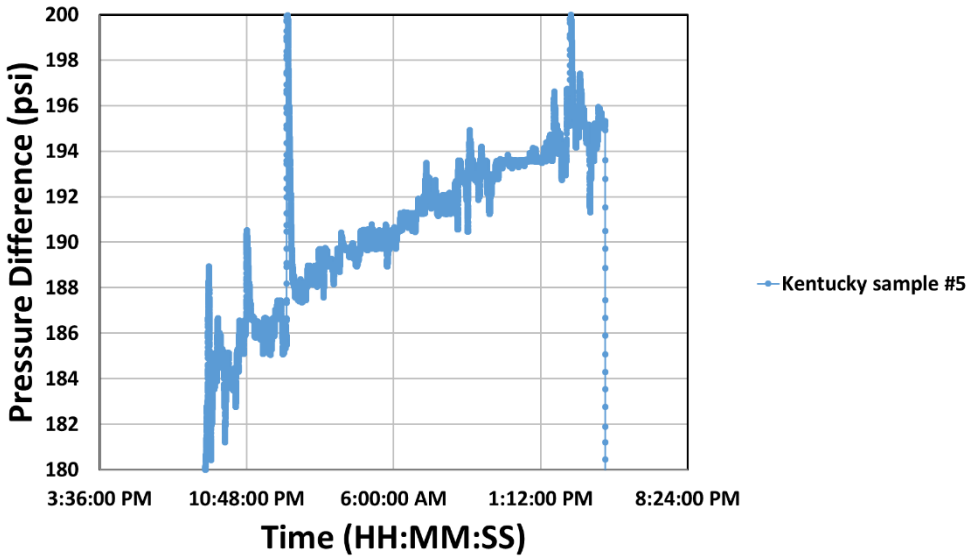

Figure 3-17: Differential pressure measured during the core flooding of Kentucky core sample 5. Here is the interval of supposedly steady-state differential pressure. A 4-psi difference is observed.

3.4 RELATIVE PERMEABILITY

Drainage relative permeability was measured using the unsteady-state technique (Heaviside and Black, 1983; Honarpour and Mahmood, 1988; Peters, 2012b; Richardson et al., 1952). The differential pressure and volume of injected and produced fluids were measured during the core flooding experiments. Because the core samples were short, the injection rate had to be high enough to eliminate capillary end-effect (Olafuyi et al., 2008). Injection rate was at 2 ml/min for the unsteady-state experiments of Berea and the BKB and KBK parallel composite cores. On the other hand, due to their much lower absolute permeabilities, the injection rate was at 10 ml/hr for the Kentucky and the BKB perpendicular composite cores, and was at 8 ml/hr for the KBK perpendicular composite core.

SCORES, a core simulator, was used to determine the relative permeability of the core samples as well as the composite cores by history matching production and pressure data (Maas et al., 2011; McPhee et al., 2015). The relative permeability table was modified until the simulated production and differential pressure data matched the experimental production and differential pressure data.

Also, the Johnson-Bossler-Naumann analytical solution (JBN method), which is an extension of the Welge solution (Johnson et al., 1959; Welge, 1952), was used to determine the relative permeability. These two solutions were based on the Buckley-Leverett approximate solution of one-dimensional immiscible displacement in a porous medium (Buckley and Leverett, 1942).

3.4.1 Berea Sandstone Core Samples

Figure 3-18 shows the production and pressure data collected during the core flooding experiment on Berea sample 14. It is an unsteady-state displacement experiment

in which brine is displaced by n-decane. This figure shows the cumulative brine production and differential pressure (downstream subtracted from upstream pressure) data over time.

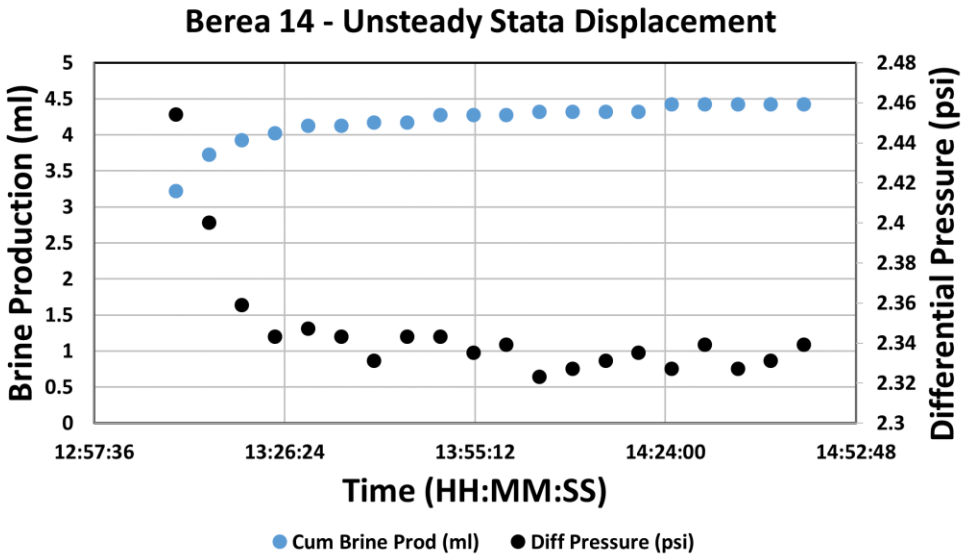

Figure 3-18: Production and pressure data of the unsteady-state displacement experiment of Berea sample 14. Cumulative brine production (blue dots) and differential pressure (black dots) data plotted over time.

Figure 3-19 shows the experimental production and pressure data along with their simulation results. The unsteady-state experiment was simulated to determine the drainage relative permeabilities of Berea sandstone. Overall, there is a good agreement between the experimental and simulated data.

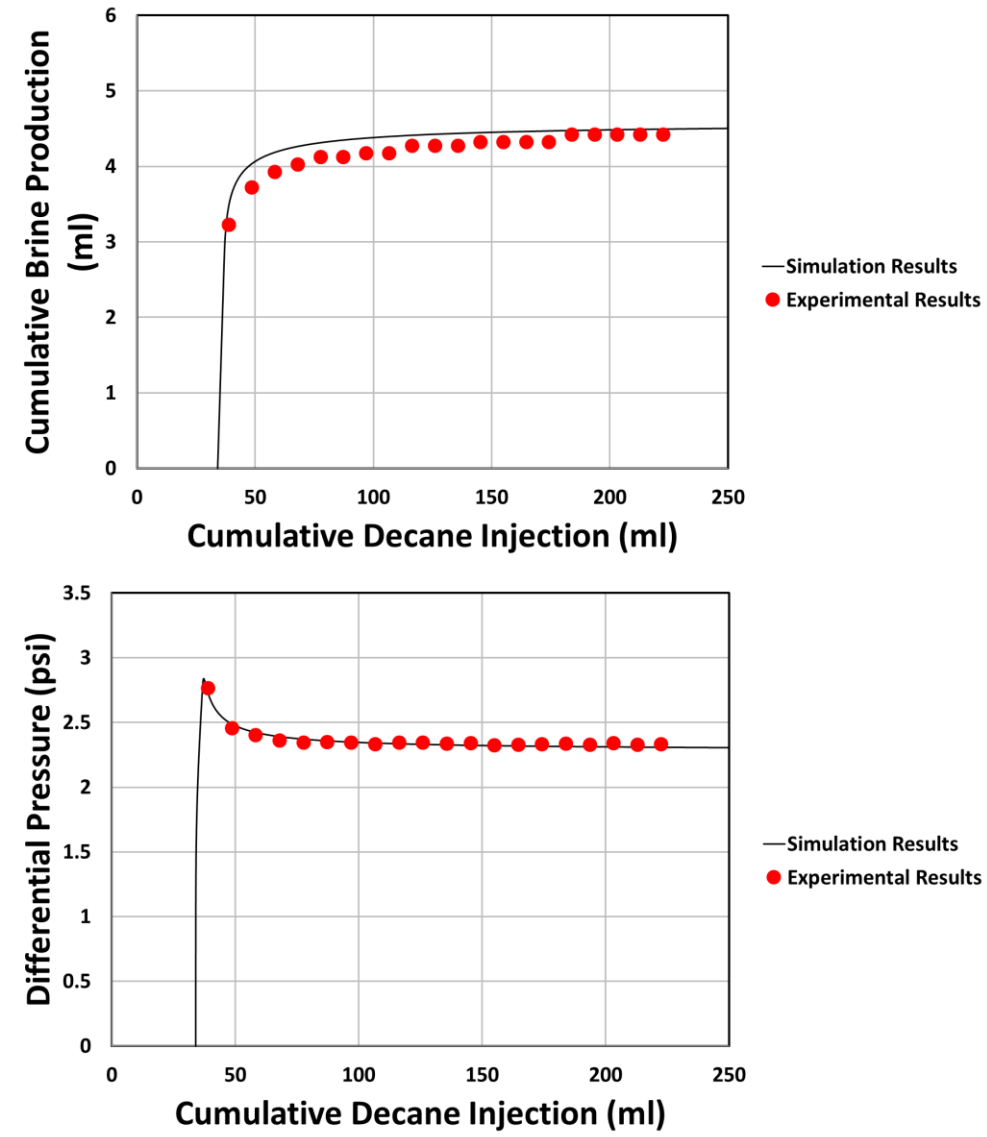

Figure 3-19: Berea sample 14 experimental cumulative brine production compared against SCORES simulation results (top) and experimental pressure difference compared against SCORES simulation results (bottom).

Figure 3-20 shows the simulated drainage relative permeability curves of Berea sandstone for both brine and n-decane. In this figure, I compare the results to steady-state Berea sandstone drainage relative permeabilities of both brine and n-decane from a previously documented study (Jordan 2016). There is a good agreement between the brine relative permeabilities; however, the n-decane relative permeability in our study is slightly lower. This is caused by the difference in irreducible water saturation. To obtain good history matching, the irreducible water saturation had to be set at 0.4. This high water saturation reflects upon the efficiency of the displacement rather than the quality of Berea sandstone. Decane is less viscous than brine, and in this case the fluids are causing this high remaining water saturation.

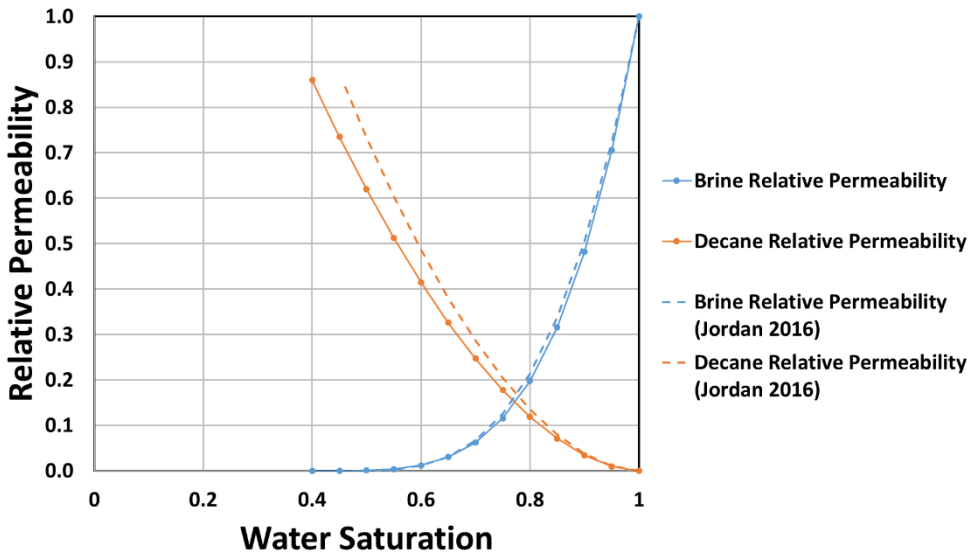

Figure 3-20: Berea sandstone relative permeabilities of brine and n-decane. Results from this study (solid lines) are in good agreement with the ones collected from a previously documented study (dashed lines) (Jordan 2016).

3.4.2 Kentucky Sandstone Core Samples

Figure 3-21 shows the production and pressure data collected during the unsteady-state displacement experiment on Kentucky sample 9. The figure shows the cumulative brine production and pressure difference over time. Figure 3-22 shows the relative permeability data calculated using the JBN method. The relative permeability data is fitted with a Brooks-Corey model.

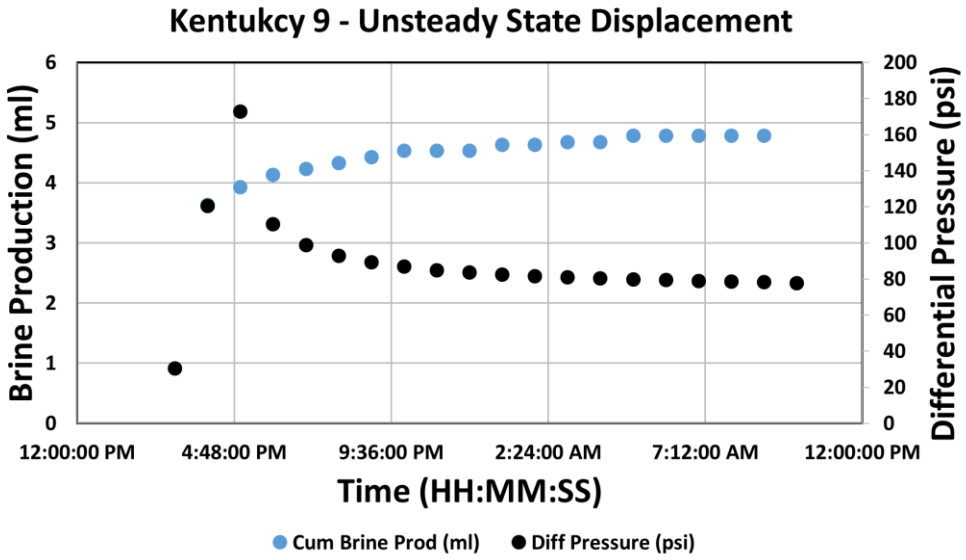

Figure 3-21: Production and pressure data of the unsteady-state displacement experiment of Kentucky sample 9. Cumulative brine production (blue dots) and differential pressure (black dots) data plotted over time.

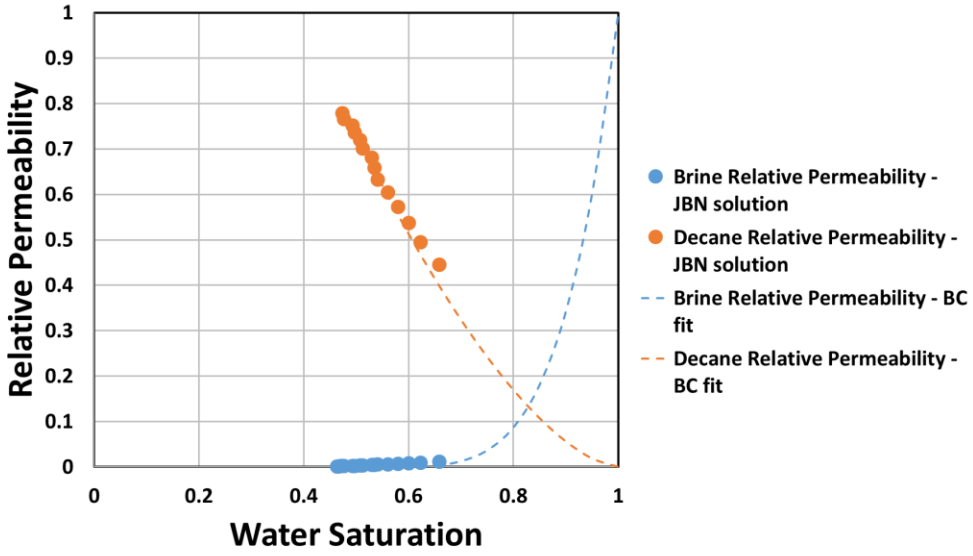

Figure 3-22: Kentucky sandstone relative permeability calculated using the JBN method fitted with a Brooks-Corey model (brine and n-decane exponents are equal to 5 and 1.6, respectively).

3.5 Mercury Intrusion Capillary Pressure

Capillary pressure of the core samples and the composite samples were measured by the MICP method. Typical values for interfacial tension and contact angle between oil and water, and air and mercury laboratory systems are tabulated in Table 3-1. Values used for this study are listed in Table 3-2.

System	Interfacial Tension, σ (mN/m)	Contact Angle, θ (degree)	σcosθ
Air-Mercury	480	140	368
Oil-Water	48	30	42

Table 3-1: Typical laboratory values for interfacial tension and contact angle of air-mercury and oil-water systems (Peters, 2012b).

System	Interfacial Tension, σ (mN/m)	Contact Angle, θ (degree)	σcosθ
Air-Mercury	485	130	≈ 312
n-Decane-Brine	53.7	30	≈ 47

Table 3-2: Interfacial tension and contact angle values used in this study. Air-mercury values were provided by Micromeritics; the n-decane-brine values are from a previously published research (Cai et al., 1996).

The Laplace's equation (equation 11) was used to calculate the distribution of the pore-throat radii of the Berea and Kentucky core samples, as well as the composite cores,

$$P_c = \frac{2\,\sigma\,|cos\theta|}{r}\ , \qquad (11)$$

where P_c is the capillary pressure, σ is the interfacial tension, θ is the contact angle, and r is the pore-throat radius.

Equation (12) can be derived from equation (11) to determine the capillary pressure of a different system or to convert from one system to another, in this case from air-mercury to n-decane-brine, knowing that the pore-throat radius, r, is the same in both systems.

$$P_{c1} = \frac{\sigma_1 \, cos\theta_1 \, P_{c2}}{\sigma_2 \, cos\theta_2} \, , \tag{12}$$

where subscript (1) refers to the n-decane-brine system and subscript (2) refers to the air-mercury system.

Capillary pressure data provide valuable petrophysical information and can be used to estimate relative permeability. Therefore, capillary pressure drainage curves were converted to relative permeability drainage using Burdine's equations (equation 13, 14, and 15) (Burdine, 1953). This approach provided relative permeability data sets that were compared with actual experimental relative permeability data. The integration was calculated numerically in these equations:

$$\overline{K_{rw}}(Sw^*) = (Sw^*)^2 \, \frac{\int_0^{Sw^*} \frac{1}{P_c^2} \, dSw^*}{\int_0^1 \frac{1}{P_c^2} \, dSw^*} \, , \tag{13}$$

$$\overline{K_{rnw}}(Sw^*) = (1 - Sw^*)^2 \, \frac{\int_{Sw^*}^1 \frac{1}{P_c^2} \, dSw^*}{\int_0^1 \frac{1}{P_c^2} \, dSw^*} \, , \tag{14}$$

and

$$Sw^* = \frac{Sw - Sw_{irr}}{1 - Sw_{irr}} \, , \tag{15}$$

where $\overline{K_{rw}}$ and $\overline{K_{rnw}}$ are the normalized wetting and non-wetting phase relative permeabilities, respectively. Sw^* is the normalized wetting phase saturation, P_c is the capillary pressure, and Sw_{irr} is the wetting phase irreducible saturation. The normalized wetting phase relative permeability is the same as the true wetting phase relative permeability; however, to obtain the true non-wetting phase relative permeability, the normalized non-wetting phase relative permeability was multiplied by K_{nwr} end-point (the non-wetting phase relative permeability end-point at the irreducible wetting phase saturation).

3.5.1 Berea Sandstone Core Samples

The following plot is for the capillary pressure curves of two Berea core samples, 1 and 5 (Figure 3-23). These data were closure corrected (conformance correction was applied). Figure 3-24 shows the calculated pore-throat radii distribution, and Figure 3-25 shows the capillary pressure curves converted from the air-mercury system to the n-decane-brine system of the same Berea core samples.

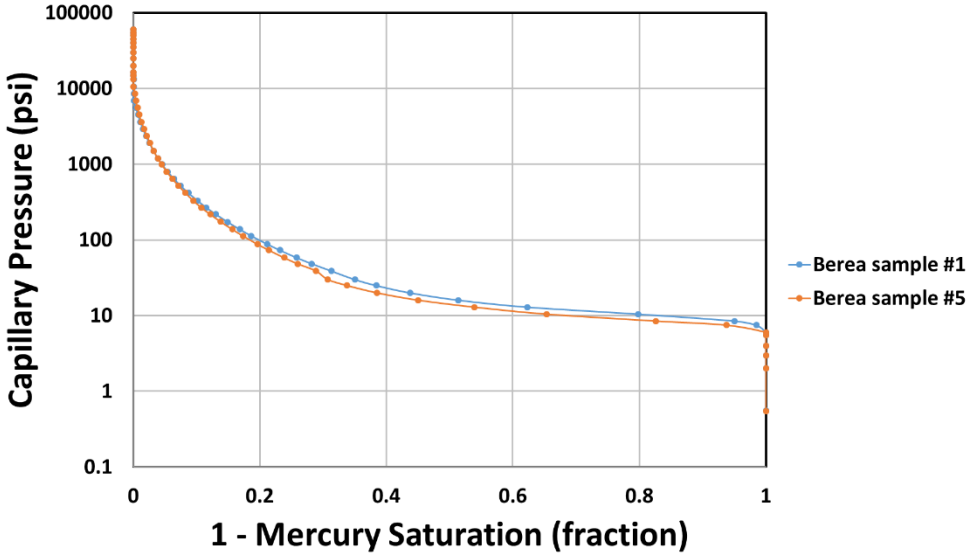

Figure 3-23: Capillary pressure curve of Berea samples 1 and 5. Pc curves were corrected for closure. The two Pc curves are almost identical.

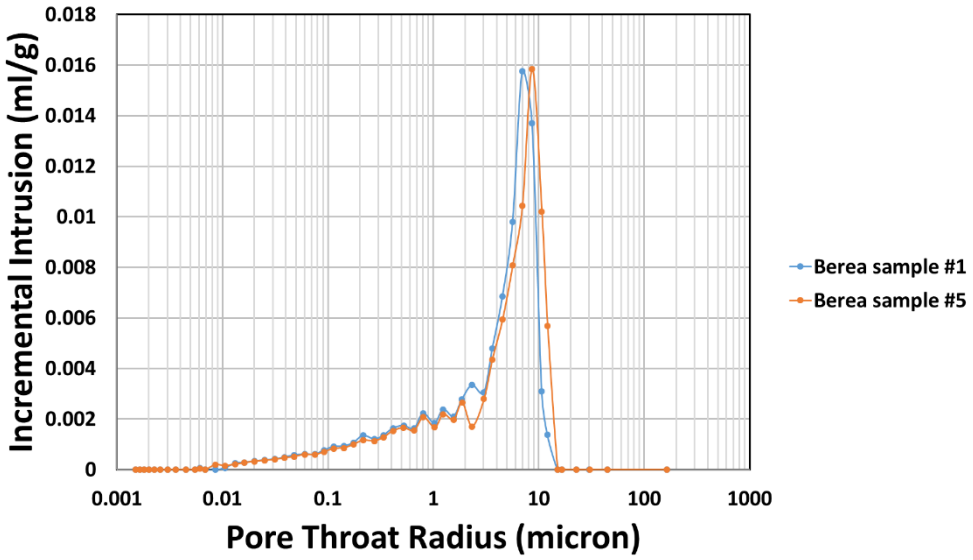

Figure 3-24: Calculated pore-throat radii distribution of Berea samples 1 and 5. Only a very slight difference exists in the dominant pore-throat radius of Berea samples 1 and 5.

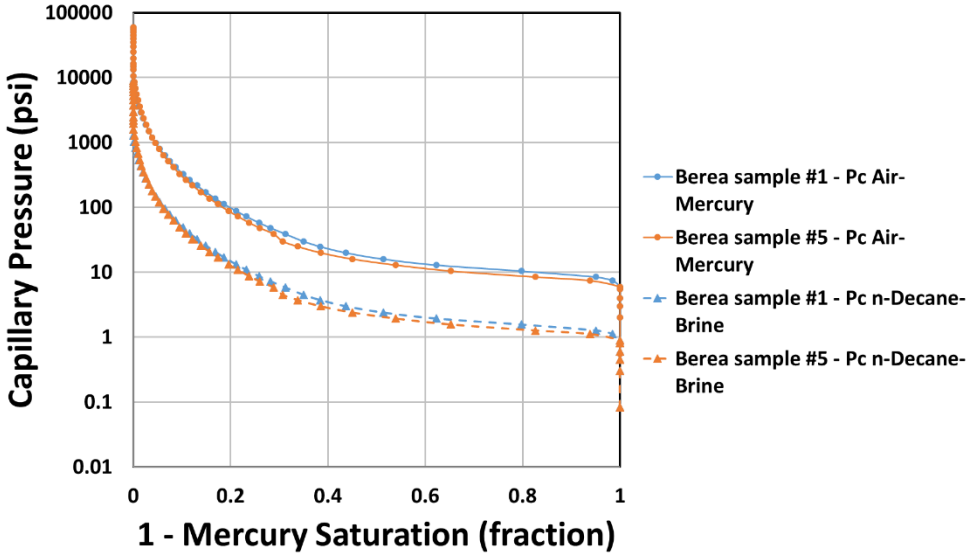

Figure 3-25: Pc curves of Berea samples 1 and 5 converted from air-mercury to n-decane-brine systems (dashed lines). Overall, capillary pressure decreased.

Using Burdine's equations (13) and (14) I calculated the drainage relative permeability curves of both the brine and n-decane from drainage capillary pressure curves. Since MICP data normally are not used for this purpose because it does not account for irreducible water saturation, the water saturation from the capillary pressure data was assumed to be the normalized water saturation (Sw^*). Then, the water saturation, Sw, was calculated using equation (15), where the Sw_{irr} was determined from the core flooding experiments of Berea core samples (n-decane displacing brine). Sw_{irr} was found to be approximately 0.5 in this research, and was found to be 0.455 in a previously documented study (Jordan, 2016).

Jordan (2016) measured the relative permeability of Berea sandstone using the steady-state method and was able to fit the data with a Brooks-Corey model using equations (16) and (17). The Brooks-Corey parameters are tabulated in Table 3-3.

Brooks-Corey Parameters	Brine	n-Decane
Brooks-Corey Exponents (n)	3.377	1.844
Irreducible Saturation (Sw_{irr})	0.455	N/A
Endpoint Relative Permeability (K_{rnw})	N/A	0.860

Table 3-3: Brooks-Corey parameters used in developing drainage relative permeability curves in Berea sandstone for both brine and n-decane (Jordan, 2016).

The Brooks-Corey drainage relative permeability models were used to fit the experimental data collected from steady-state measurements (Jordan, 2016), via

$$K_{rw} = \left(\frac{Sw - Sw_{irr}}{1 - Sw_{irr}}\right)^{n_w} , \tag{16}$$

and

$$K_{rnw} = K_{rnw}@Sw_{irr} \left(\frac{1 - Sw}{1 - Sw_{irr}}\right)^{n_{nw}} , \tag{17}$$

where K_{rw} and K_{rnw} are the water saturation dependent relative permeabilities of the wetting and non-wetting phases, respectively. Sw is the water saturation (the wetting phase), Sw_{irr} is the irreducible water saturation, $K_{rnw}@Sw_{irr}$ is the endpoint relative permeability of the non-wetting phase, and $n_w$and n_{nw} are the Brooks-Corey exponents (fitting parameters) of the wetting and non-wetting phases, respectively.

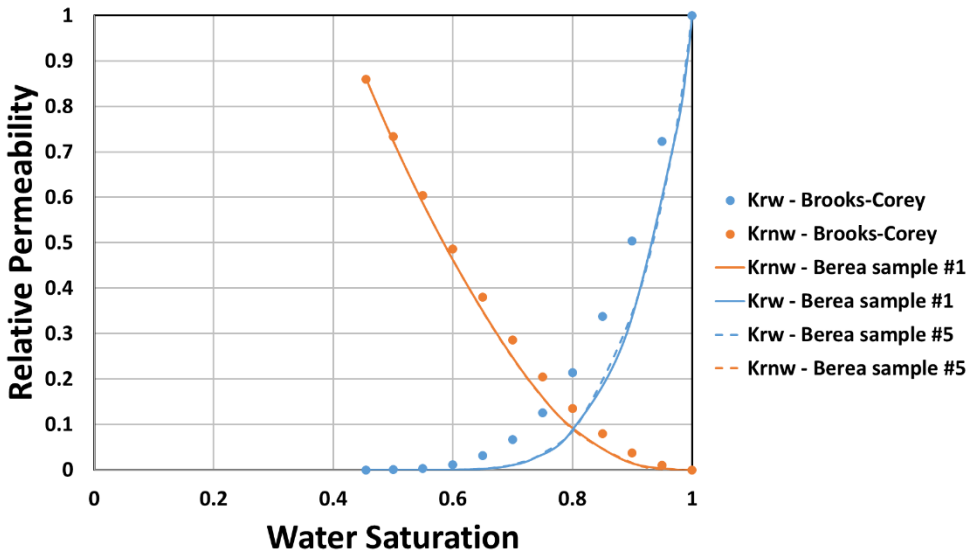

Figure 3-26: Calculated drainage relative permeability curves from the capillary pressure data of Berea core samples 1 and 5. Relative permeability to brine and n-decane is shown, in blue and orange, respectively. The relative permeabilities calculated using Brooks-Corey model are shown by dots (Jordan, 2016). A good agreement exists between the two data sets.

3.5.2 Kentucky Sandstone Core Samples

The following plot is for the capillary pressure curves of two Kentucky core samples 4 and 6 (Figure 3-27). These data were closure corrected (conformance correction was applied). Figure 3-28 shows the calculated pore-throat radii distribution of the same Kentucky core samples (4 and 6), and Figure 3-29 shows the capillary pressure curves converted from the air-mercury system to the n-decane-brine system.

Calculated relative permeability curves from the capillary pressure data are presented in Figure 3-30. The Sw_{irr} and K_{rnw} end-points from the core flooding of the Kentucky core samples were found to be nearly 0.5 and 0.8, respectively.

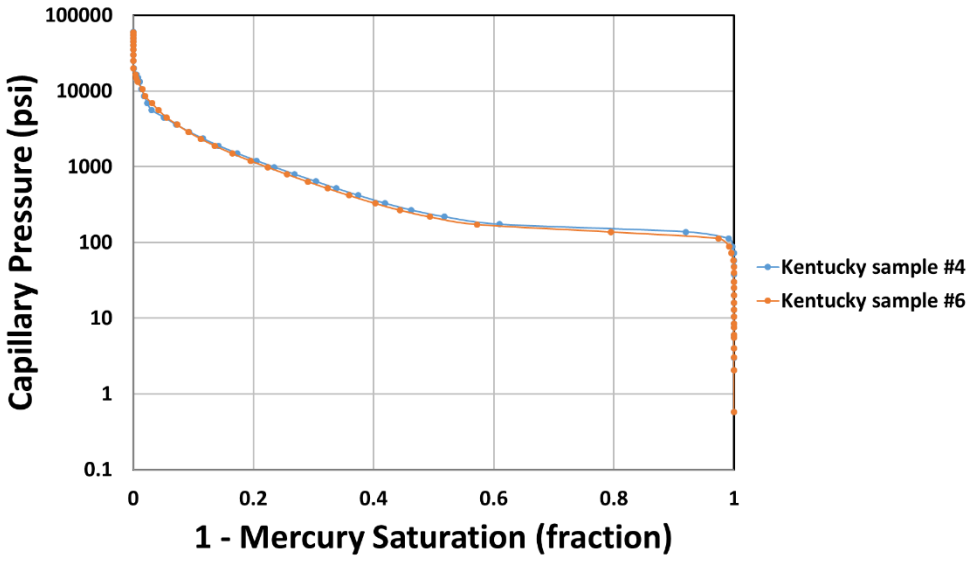

Figure 3-27: Capillary pressure curves of Kentucky samples 4 and 6. These Pc curves were corrected for closure, and are almost identical.

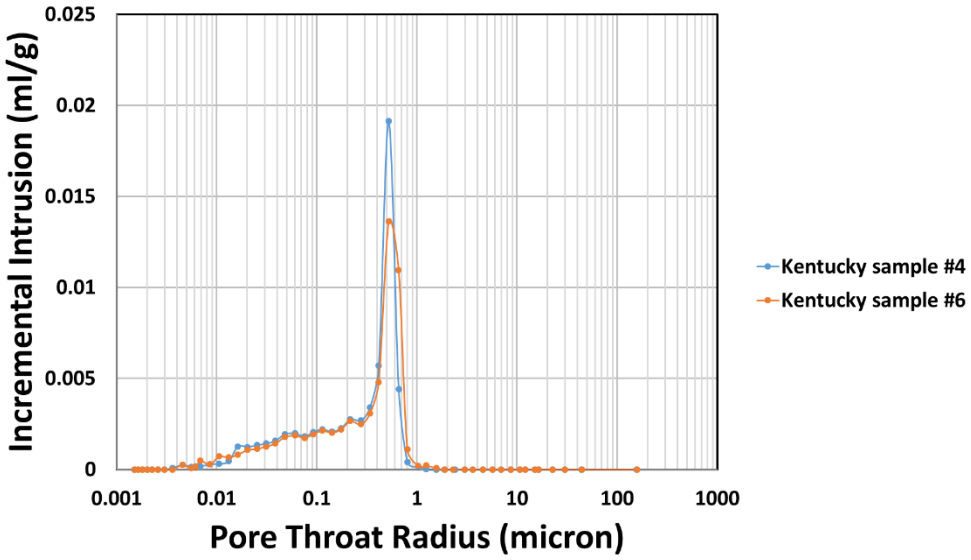

Figure 3-28: Calculated pore-throat radii distribution of Kentucky samples 4 and 6.

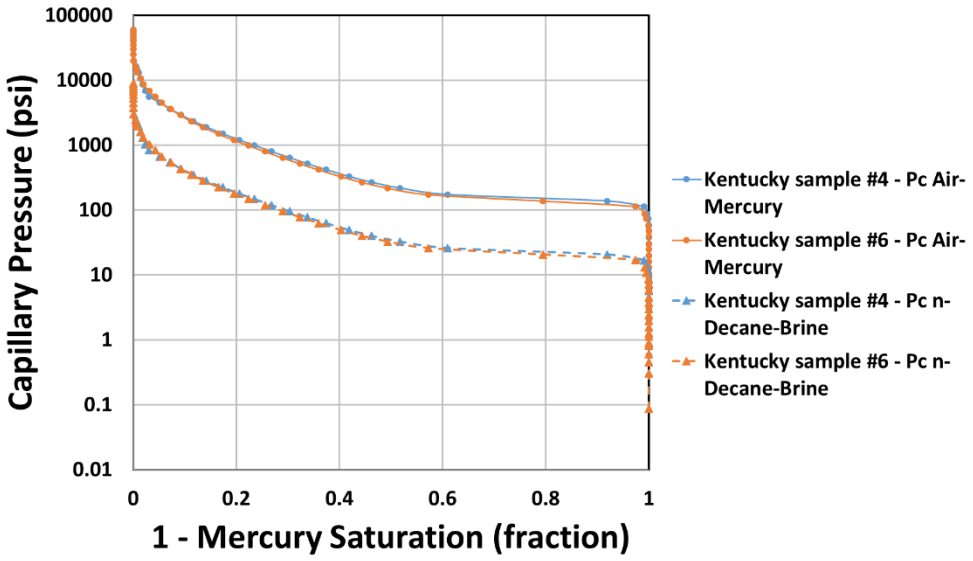

Figure 3-29: Pc curves of Kentucky samples 4 and 6 converted to from air-mercury to n-decane-brine systems (dashes). Overall, capillary pressure decreased.

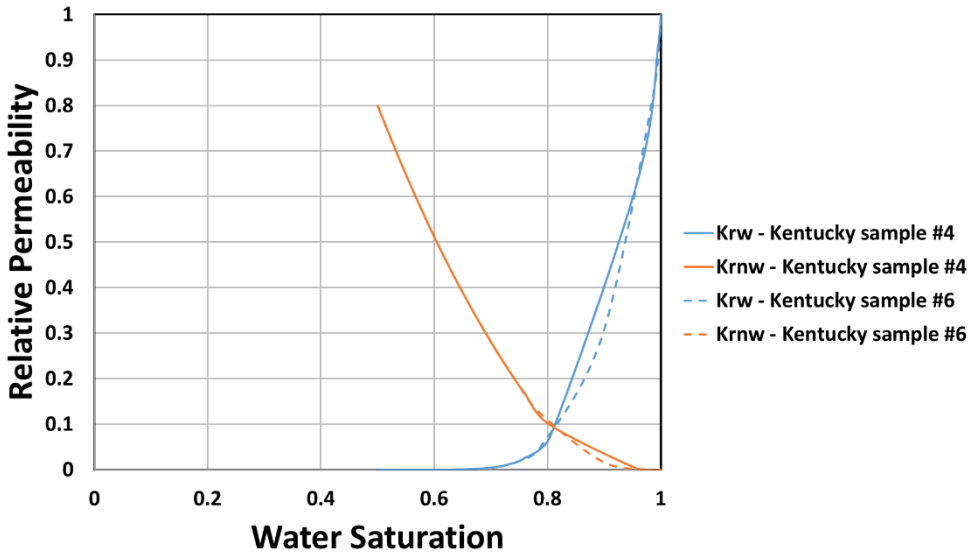

Figure 3-30: Calculated drainage relative permeability curves from the capillary pressure data of Kentucky core samples 4 and 6. Relative permeabilities to brine and n-decane are shown in blue and orange, respectively.

3.6 PARALLEL FLOW

3.6.1 Absolute Permeability

Absolute permeabilities of the parallel composite cores, BKB and KBK, were measured (calculated) and cross-checked using the arithmetic average of the permeability of the individual core samples.

In layers arranged in parallel (parallel-layered system), where the layers are of equal thickness, the total system permeability is equal to the arithmetic average of the individual permeability of the layers (Ahmed, 2010; Bear, 1988), and it can be computed via

$$K_{avg} = \frac{1}{n} \sum_{i=1}^{n} K_i \ , \tag{18}$$

where K_{avg} is the average absolute permeability of the system, n is the total number of layers, and K_i is the absolute permeability of the i_{th} layer.

The absolute permeabilities of the composite cores, BKB and KBK, were 207 and 110 mD, respectively. It was calculated using Darcy's law and then cross-checked against the arithmetic average of the individual permeability of each rock in the composite samples. The arithmetic averages of the BKB and KBK composite cores are 200 and 100 mD, respectively; this resulted in differences of 3.71 and 9.85%, respectively, between the average and experimental permeabilities (Figures 3-31 and 3-32).

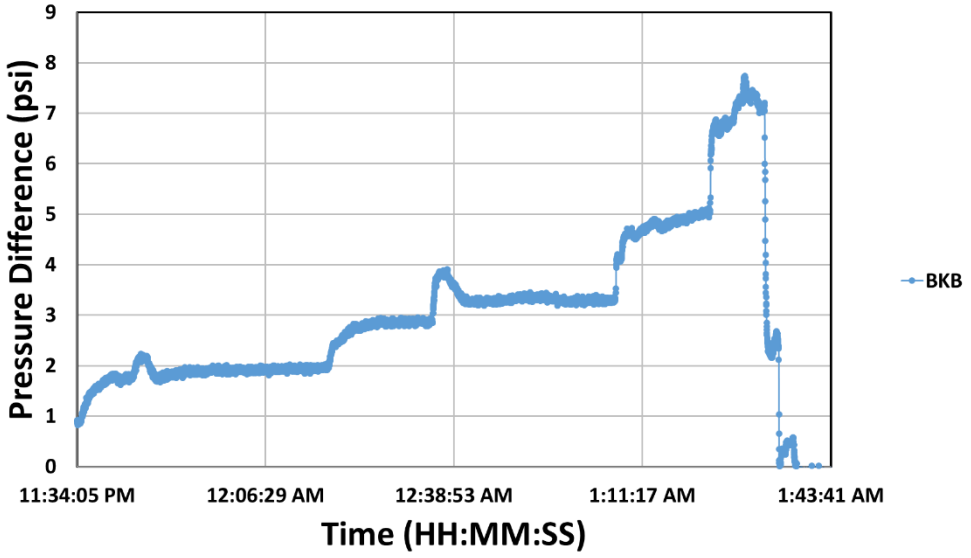

Figure 3-31: Core flooding differential pressure data versus time for the BKB composite cores at multiple rates. Calculated permeability is 207 mD, whereas the arithmetic average is 200 mD (a difference of 3.71%).

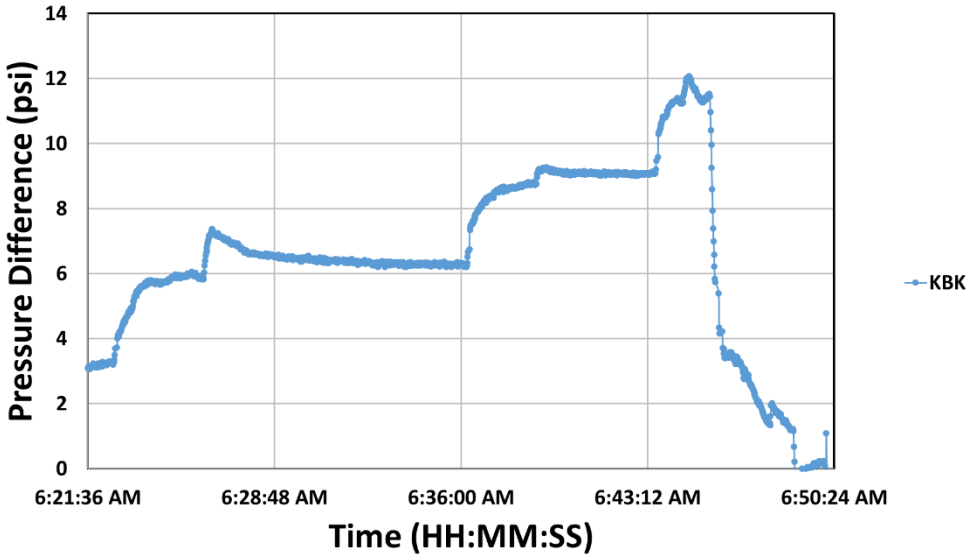

Figure 3-32: Core flooding differential pressure data versus time for the KBK composite cores at multiple rates. Calculated permeability is 110 mD, whereas the arithmetic average is 100 mD (a difference of 9.85%).

3.6.2 Relative Permeability – Drainage

Figure 3-33 shows the production and pressure data for the unsteady-state displacement of the BKB parallel composite sample, and Figure 3-34 shows the calculated relative permeability of the BKB composite sample using the JBN method, fitted with a Brooks-Corey model.

The data collected from the unsteady-state displacement of the KBK parallel composite sample was not reliable. I believe that the sample failed during the process, and therefore the production and pressure data collected were not feasible to use in calculating the composite's relative permeabilities.

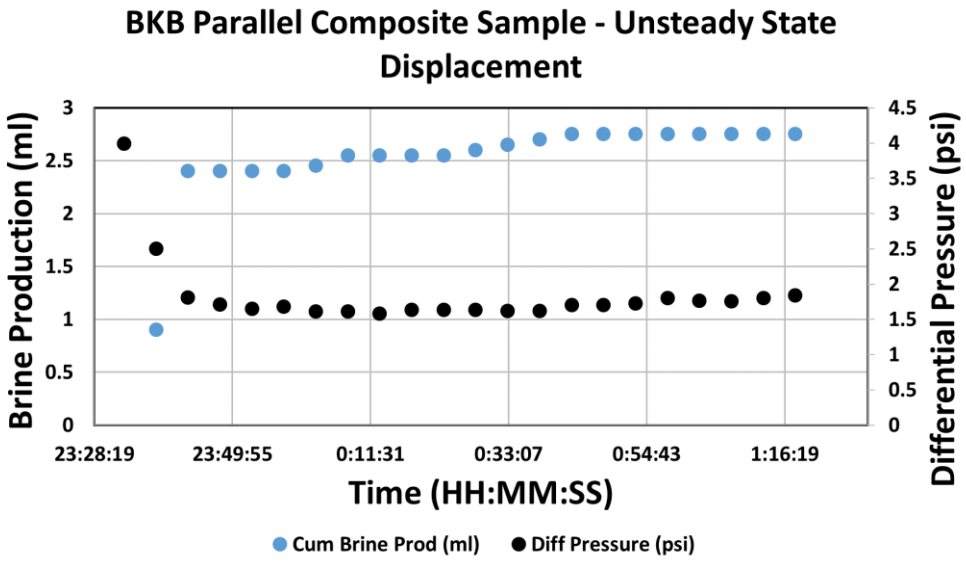

Figure 3-33: Production and pressure data of the unsteady-state displacement experiment of the BKB parallel composite sample. Cumulative brine production (blue dots) and differential pressure (black dots) data are plotted over time.

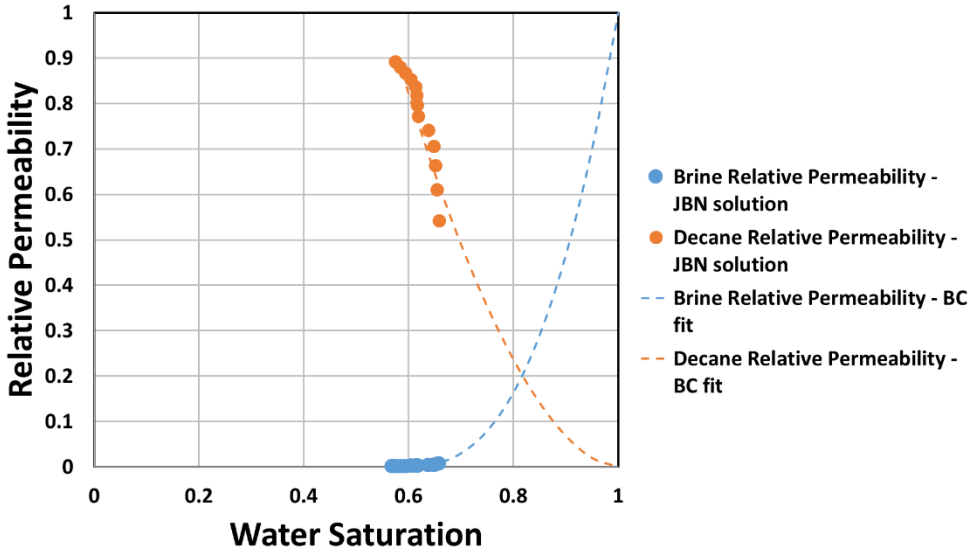

Figure 3-34: BKB parallel composite sample relative permeability calculated using the JBN method fitted with a Brooks-Corey model (brine and n-decane exponents are equal to 2.8 and 1.8, respectively).

3.6.3 Capillary Pressure

Capillary pressure of the composite cores, BKB and KBK, were measured. Figure 3-35 shows the capillary pressure curves versus saturation of the wetting phase of two fluid systems, air-mercury and n-decane-brine, for both BKB and KBK composite cores. The entry pressure into the BKB and KBK composite cores is almost the same. This reflects the entry into the Berea component of these two parallel composite cores. There is a slight signature of a second entry into both composite cores; however, in the BKB composite core, it happens at around 0.6, whereas in the KBK it appears at around 0.9 of wetting phase saturation. This could represent the entry of mercury into the Kentucky component of that system. These two systems being parallel and open to mercury intrusion are represented by a bi-modal pore-throat distribution (Figure 3-36).

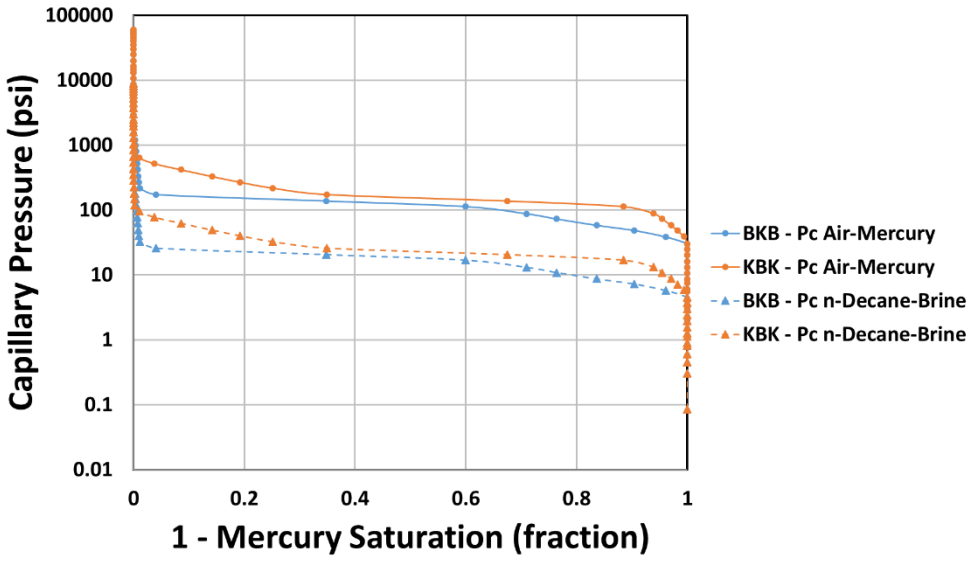

Figure 3-35: Pc curves of the BKB (blue) and KBK (orange) parallel composite cores converted from air-mercury (solid lines) into n-decane-brine systems (dashed lines). They both exhibit two entry pressures (bi-modality).

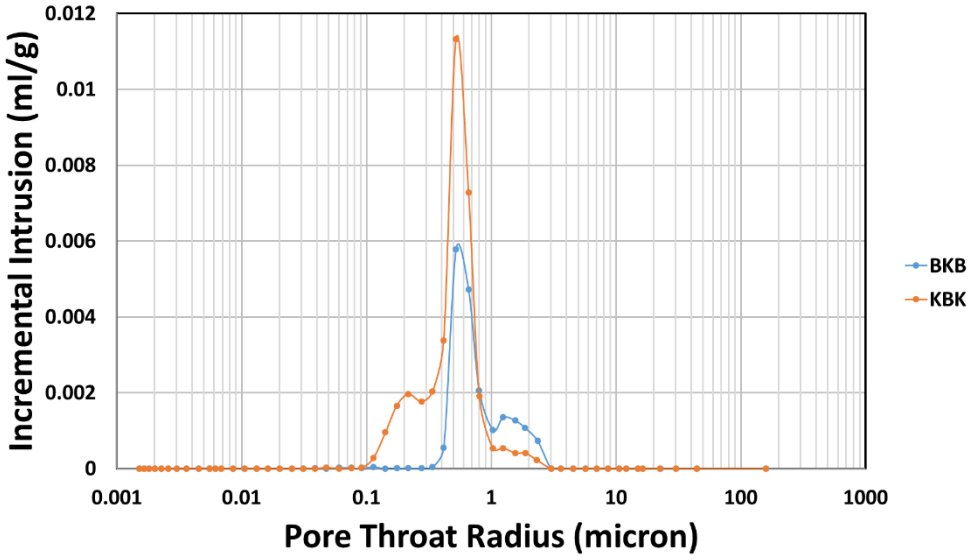

Figure 3-36: Calculated pore-throat radii distribution of the BKB (blue) and KBK (orange) parallel composite cores. Bi-modality is observed in both composite cores.

3.7 PERPENDICULAR FLOW

3.7.1 Absolute Permeability

Absolute permeabilities of the composite cores, BKB and KBK, were measured and cross-checked using the harmonic average.

In layers arranged in series, where the layers are of equal length, the total system permeability is equal to the harmonic average of the individual permeability of the layers (Ahmed, 2010; Bear, 1988), and it can be computed via

$$K_{avg} = \frac{n}{\sum_{i=1}^{n} \frac{1}{K_i}}, \tag{19}$$

where K_{avg} is the average absolute permeability of the system, n is the total number of layers, and K_i is the absolute permeability of the i_{th} layer.

The absolute permeabilities of the composite cores, BKB and KBK, were 0.40 and 0.25 mD, respectively. It was calculated using Darcy's law and then cross-checked against the harmonic average of the individual permeability of each rock in the composite samples. The harmonic averages of the BKB and KBK composite cores are 0.54 and 0.27 mD, respectively; this resulted in differences of 25 and 6%, respectively, between the average and experimental permeabilities (Figures 3-37 and 3-38).

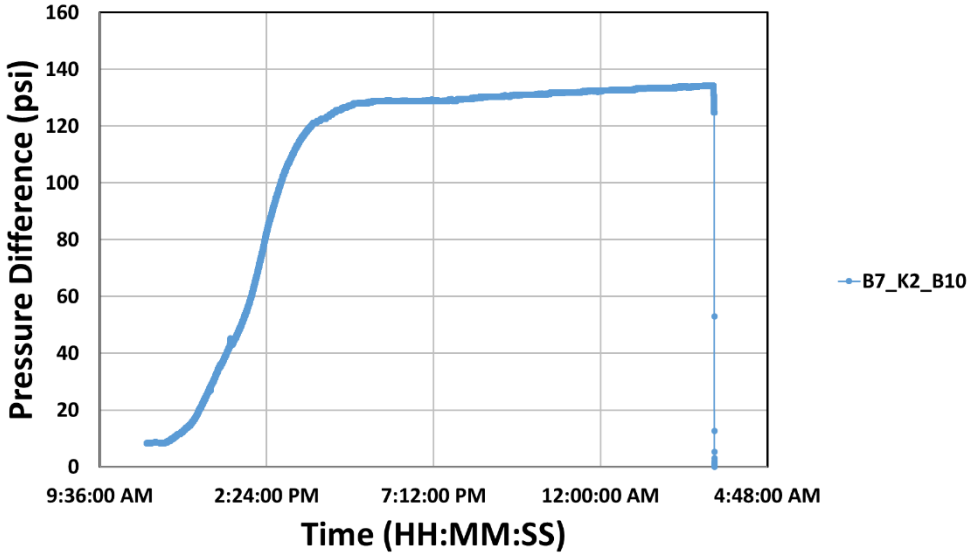

Figure 3-37: Core flooding differential pressure data versus time for the BKB perpendicular composite cores. Calculated permeability is 0.40 mD, whereas the harmonic average is 0.54 mD (a difference of 25%).

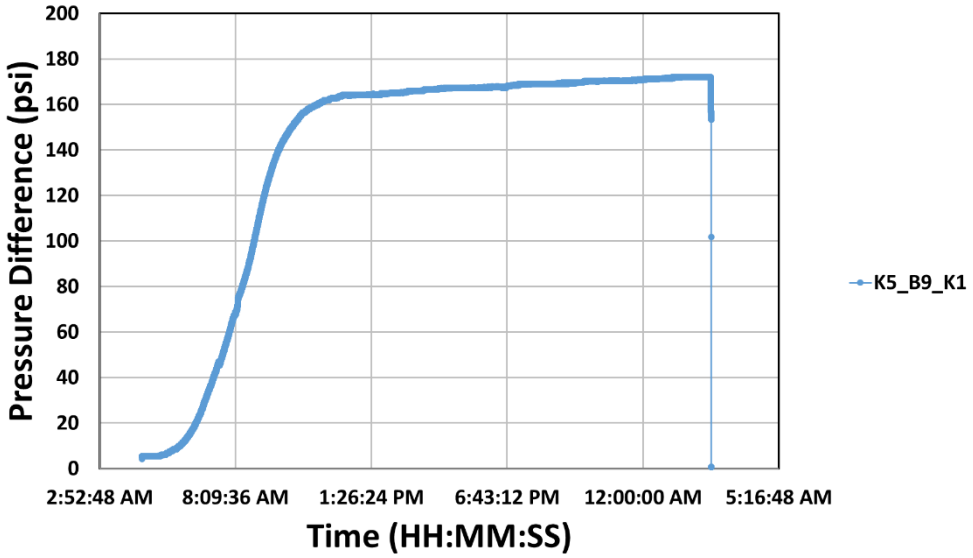

Figure 3-38: Core flooding differential pressure data versus time for the KBK perpendicular composite cores. Calculated permeability is 0.25 mD, whereas the harmonic average is 0.27 mD (a difference of 6%).

3.7.2 Relative Permeability – Drainage

Figure 3-39 shows the production and pressure data for the unsteady-state displacement of the BKB perpendicular composite sample, and Figure 3-40 shows the calculated relative permeabilities of the composite sample. The relative permeabilities of both brine and n-decane are lower compared to the BKB parallel composite sample.

The pressure data for the unsteady-state displacement of the KBK perpendicular composite sample were too high to be recognized by the pressure sensor used. The sensor has an upper pressure limit of 300 psi, and the actual experiment exceeded this limit.

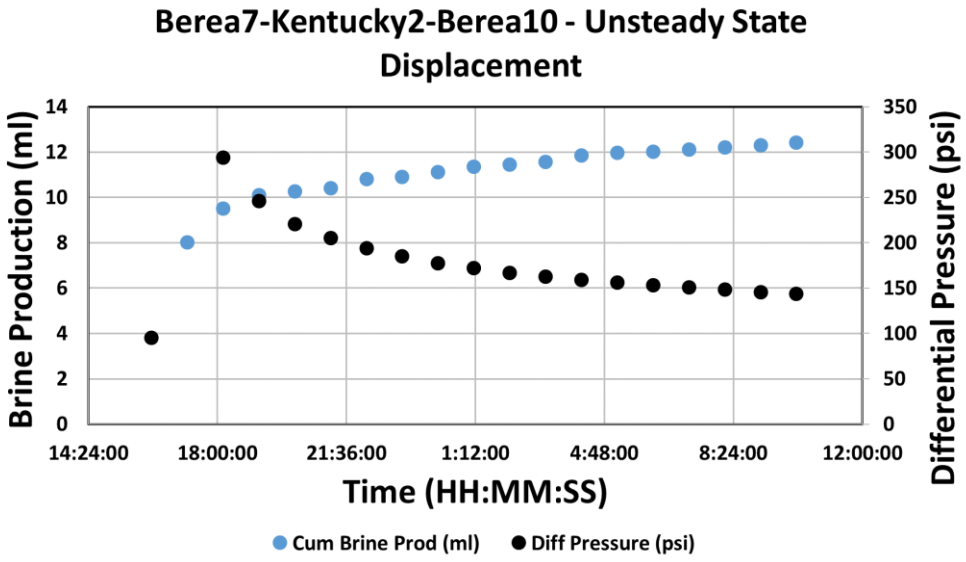

Figure 3-39: Production and pressure data of the unsteady-state displacement experiment of the BKB perpendicular composite sample. Cumulative brine production (blue dots) and differential pressure (black dots) data plotted over time.

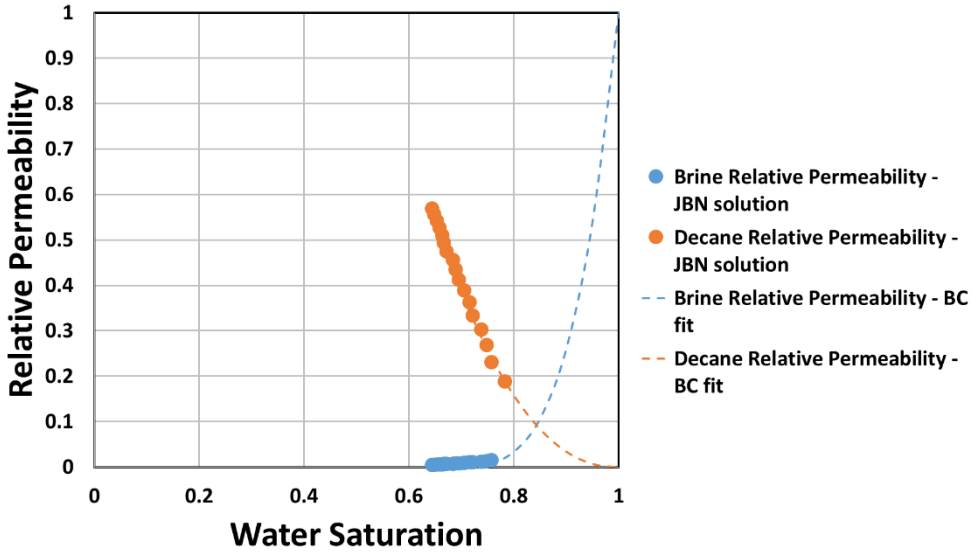

Figure 3-40: BKB perpendicular composite sample relative permeability calculated using the JBN method fitted with a Brooks-Corey model (brine and n-decane exponents are equal to 4 and 2.2, respectively).

3.7.3 Capillary Pressure

Capillary pressures of the perpendicular composite cores, BKB and KBK, were measured. Figure 3-41 shows the capillary pressure curves of these two composite samples. The BKB composite core capillary pressure curve shows only one entry pressure. This sample is arranged in series and therefore a second entry pressure into the Kentucky component of the system should have been observed. In the KBK composite sample, there is a sign of early intrusion. The Berea component in this system was supposed to be overshadowed by the high capillary pressure into the Kentucky components. Figure 3-42 shows the incremental intrusion of mercury into both composite samples.

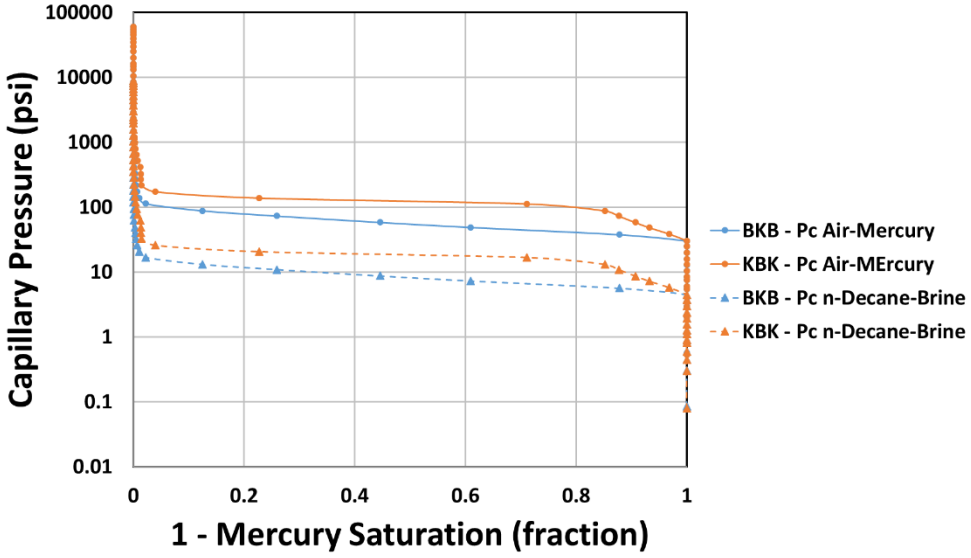

Figure 3-41: Pc curves of the BKB (blue) and KBK (orange) perpendicular composite cores converted from air-mercury (solid lines) into n-decane-brine systems (dashed lines).

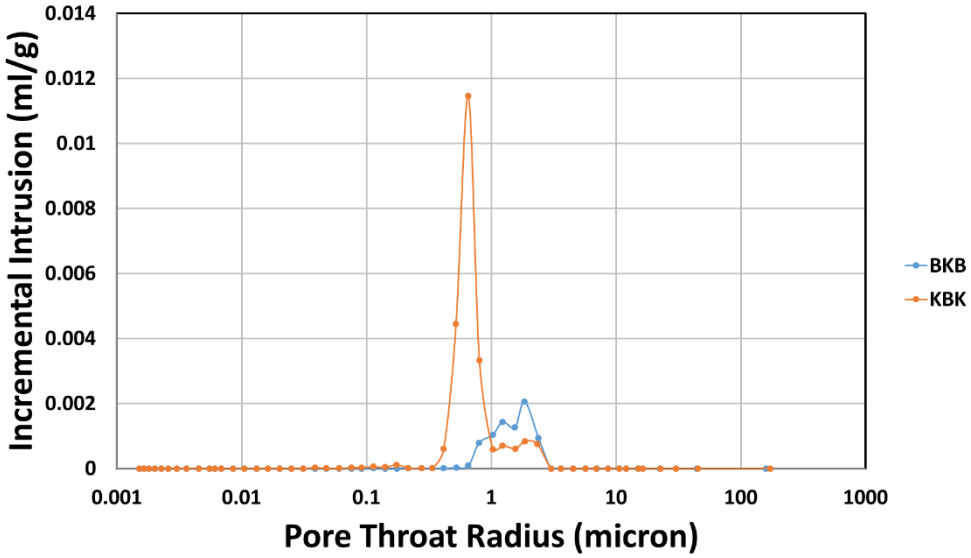

Figure 3-42: Calculated pore-throat radii distribution of the BKB (blue) and KBK (orange) perpendicular composite cores.

Chapter 4 – Conclusions

In this chapter, I state the conclusions resulting from, and the limitations and uncertainties of, this research. Suggestions for future work and recommendations are presented.

4.1 SUMMARY

MICP and relative permeability experiments were conducted to measure the aforementioned petrophysical properties in the BKB and KBK composite core samples in two flow conditions, parallel and normal. The individual petrophysical properties of the system components, Berea and Kentucky sandstone core samples, were also measured beforehand, to set the reference for the composite cores petrophysical properties.

This study's workflow started with first obtaining micro-CT images of the samples to ensure their physical integrity and absence of micron-scale fractures. Later, NMR analysis was performed to obtain the samples' NMR porosities and pore-size distributions. The same was done for the composite cores, BKB and KBK. Next, the absolute permeabilities of the individual and the composite samples were measured and calculated. Finally, the relative permeabilities and capillary pressure of the individual and composite core samples were measured.

The Berea and Kentucky composite cores were fabricated to allow for testing them in parallel and normal flow conditions. The fabrication techniques worked, and feasible data were collected. Capillary pressure of the BKB and KBK, parallel and perpendicular, composite cores were measured, as well as their absolute permeabilities and relative permeabilities.

Figure 4-1 shows the relative permeabilities of the BKB parallel and perpendicular composite cores. The parallel system has a higher n-decane relative permeability than does the perpendicular system. In addition, the amount of remaining water saturation after core flooding was lower in the parallel system. However, the brine relative permeabilities for both is roughly the same.

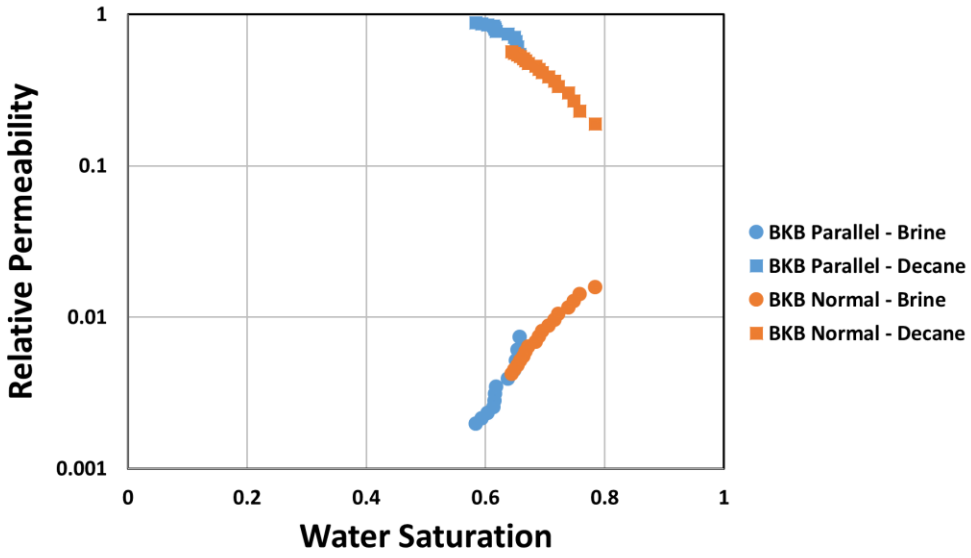

Figure 4-1: Relative permeability of the BKB composite cores in both parallel (blue) and perpendicular (orange) arrangements. The decane relative permeability of the parallel composite core samples is higher than that of the perpendicular composite core samples, whereas the brine relative permeabilities is approximately the same for both.

4.2 Limitations and Uncertainties

Relative permeability measurements have higher uncertainties than the other experiments conducted in this study. They are very sensitive to the amount of fluid volumes, whether the fluids remain in the core flooding system or are produced. The rate

of injection is a crucial factor as well. Capillary-end effect is in play in these experiments given the length of the samples. In this study, I conducted multiple experiments for multiple samples, which meant that the core flooding setup was dismantled and assembled many times. This introduces air into the system, as well as, new fluids being mixed with old fluids from previous experiments.

The fabrication techniques used also add uncertainty to the results. Different methods were attempted to fabricate the parallel and perpendicular composite samples. In the MICP samples, epoxy and heat shrink tubes were used to seal and bind the samples together. In the permeability and relative permeability samples, heat shrink tubes were used to seal and bind the samples together. There was a doubt of whether perfect seal and bind were achieved.

Cutting the samples to fabricate the parallel composite samples was challenging. The saw that was used was more applicable to large samples than to small samples. In addition, the smaller that the core samples were cut, the more fragile they became, and thus they were more easily broken during the experimental process.

4.3 Future Work and Recommendations

To eliminate capillary end effect, the injection rate and sample length can be altered. I would recommend using a pressure transducer that can transmit higher pressures, in the range of 1,000 to 2,000 psi. Having this capability allows for the injection rate to be high, especially in the low-permeability rock samples. Otherwise, longer samples should be used (approximately 1 ft. long) for relative permeability measurements. Moreover, the use of steady-state instead of unsteady-state displacement would potentially yield more

reliable results, and relative permeability curves in a wider range of water saturation would be established.

Naturally-laminated samples rather than fabricated ones should be used. Rocks that are naturally formed and cemented would be the best option for such research. What would be more interesting is to core and cut samples from a laminated setting that is similar to the setting shown in Figure 4-2. This would be the ideal case, where core samples can be taken from the first and last layers, sandstones 1 and 2, and laminated core samples can be taken from the center, layers 2 to 7, parallel and perpendicular to laminations.

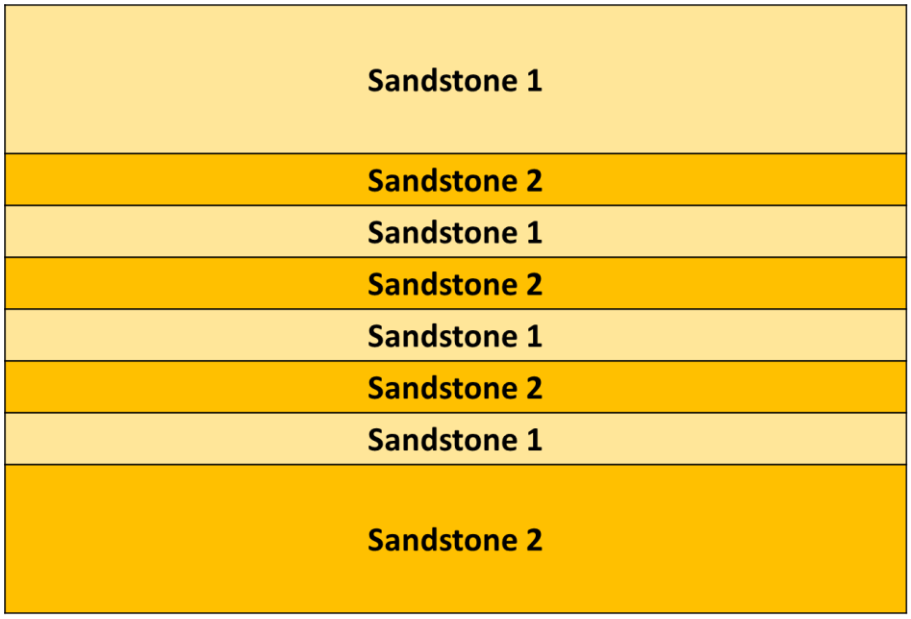

Figure 4-2: Ideal laminated setting for a future study. Laminated samples should be cut in different directions (parallel and perpendicular to bedding planes) from layers 2 to 7. Non-laminated samples should be cut from layers 1 and 2.

The MICP measurements of the composite samples should be retaken. The intrusions of mercury in the composite core samples were not representative of the Berea and Kentucky individual mercury intrusions. The stem volume used in these measurements were sometimes lower than what is recommended for a viable MICP test. The amount of stem volume should also account for the pore volumes of the composite core samples. In addition, the settings of the MICP test should allow for a longer equilibration time (45 seconds instead of 10 seconds for both the low and high analyses).

Finally, the micro-CT images that were obtained from Berea and Kentucky sandstone core samples should be used to build a layered three-dimensional small-scale models, and to numerically simulate two-phase flow and transport properties. Building small-scale models to understand the petrophysical properties through pore-scale simulation could lead to interesting results.

References

Ahmed, T., 2010. Reservoir Engineering Handbook, 4th ed. Gulf Professional Publishing, Burlington, MA, USA.

Bear, J., 1988. Dynamics of Fluids in Porous Media, Republication. ed. Dover.

Buckley, S.E., Leverett, M.C., 1942. Mechanism of Fluid Displacement in Sands. Transactions of the AIME 146, 107–116. https://doi.org/10.2118/942107-G

Burdine, N.T., 1953. Relative Permeability Calculations From Pore Size Distribution Data. Journal of Petroleum Technology 5, 71–78. https://doi.org/10.2118/225-G

Cai, B.-Y., Yang, J.-T., Guo, T.-M., 1996. Interfacial Tension of Hydrocarbon + Water/Brine Systems under High Pressure. J. Chem. Eng. Data 41, 493–496. https://doi.org/10.1021/je950259a

Corbett, P.W.M., Ringrose, P.S., Jensen, J.L., Sorbie, K.S., 1992. Laminated Clastic Reservoirs: The Interplay of Capillary Pressure and Sedimentary Architecture. Presented at the SPE Annual Technical Conference and Exhibition, Society of Petroleum Engineers. https://doi.org/10.2118/24699-MS

Corey, A.T., Rathjens, C.H., 1956. Effect of Stratification on Relative Permeability. Journal of Petroleum Technology 8, 69–71. https://doi.org/10.2118/744-G

Decane [WWW Document], n.d. Decane Physical and Chemical Properties. URL https://pubchem.ncbi.nlm.nih.gov/compound/15600 (accessed 9.21.18).

Density of Sodium Chloride Solutions [WWW Document], n.d. URL http://butane.chem.uiuc.edu/pshapley/genchem1/l21/1.html (accessed 9.21.18).

Dunn, K.J., Bergman, D.J., LaTorraca, G.A., 2002. Nuclear Magnetic Resonance Petrophysical and Logging Application, 1st ed. Pergamon.

Equilibar Research Series Back Pressure Regulators [WWW Document], n.d. . Precision Back Pressure Regulators and more. URL https://www.equilibar.com/back-pressure-regulators/research-back-pressure-regulators/ (accessed 9.22.18).

Heaviside, J., Black, C.J.J., 1983. Fundamentals of Relative Permeability: Experimental and Theoretical Considerations. Presented at the SPE Annual Technical Conference and Exhibition, Society of Petroleum Engineers. https://doi.org/10.2118/12173-MS

Honarpour, M., Koederitz, L., Harvey, A.H., 1986. Relative Permeability of Petroleum Reservoirs. C.R.C. Press, Boca Raton, Florida.

Honarpour, M., Mahmood, S.M., 1988. Relative-Permeability Measurements: An Overview. Journal of Petroleum Technology 40, 963–966. https://doi.org/10.2118/18565-PA

Honarpour, M.M., Cullick, A.S., Saad, N., 1994. Influence of Small-Scale Rock Laminations on Core Plug Oil/Water Relative Permeability and Capillary Pressure. Presented at the University of Tulsa Centennial Petroleum Engineering Symposium, Society of Petroleum Engineers. https://doi.org/10.2118/27968-MS

Honarpour, M.M., Cullick, A.S., Saad, N., Humphreys, N.V., 1995. Effect of Rock Heterogeneity on Relative Permeability: Implications for Scale-up. Journal of Petroleum Technology 47, 980–986. https://doi.org/10.2118/29311-PA

Johnson, E.F., Bossler, D.P., Bossler, V.O.N., 1959. Calculation of Relative Permeability from Displacement Experiments.

Jordan, P., 2016. Two-Phase Relative Permeability Measurements in Berea Sandstone at Reservoir Conditions. MSE thesis, The University of Texas at Austin.

Kestin, J., Khalifa, H.E., Correia, R.J., 1981. Tables of the dynamic and kinematic viscosity of aqueous NaCl solutions in the temperature range 20–150 °C and the pressure range 0.1–35 MPa. Journal of Physical and Chemical Reference Data 10, 71–88. https://doi.org/10.1063/1.555641

Lake, L.W., Johns, R.T., Rossen, W.R., Pope, G.A., 2014. Fundamentals of Enhanced Oil Recovery. Society of Petroleum Engineers, USA.

Maas, J.G., Flemisch, B., Hebing, A., 2011. Open Source Simulator Dumux Available for Scal Data Interpretation. Presented at the International Symposium of the Society of Core Analysts, p. 12.

Mahmoud, M.A., Nasr-El-Din, H.A., Wolf, D., A, C., 2015. High-Temperature Laboratory Testing of Illitic Sandstone Outcrop Cores With HCl-Alternative Fluids. SPE Production & Operations 30, 43–51. https://doi.org/10.2118/147395-PA

McPhee, C., Reed, J., Zubizarreta, I., 2015. Core Analysis: A Best Practice Guide, 1st ed. Elsevier.

Olafuyi, O.A., Cinar, Y., Knackstedt, M.A., Pinczewski, W.V., 2008. Capillary Pressure and Relative Permeability of Small Cores. Presented at the SPE Symposium on Improved Oil Recovery, Society of Petroleum Engineers. https://doi.org/10.2118/113386-MS

Ozbek, H., Fair, J.A., Phillips, S.L., 1977. Viscosity of Aqueous Sodium Chloride Solutions from 0 - 150 degC. Presented at the American Chemical Society 29th Southeast Regional Meeting, Tampa, FL.

Peng, S., Zhang, T., Loucks, R.G., Shultz, J., 2017. Application of mercury injection capillary pressure to mudrocks: Conformance and compression corrections. Marine and Petroleum Geology 88, 30–40. https://doi.org/10.1016/j.marpetgeo.2017.08.006

Peters, E., 2012a. Advanced Petrophysics, First Edition. ed. Vol. 1. Live Oak Book Company, Austin, Texas.

Peters, E., 2012b. Advanced Petrophysics, First Edition. ed. Vol. 2. Live Oak Book Company, Austin, Texas.

Richardson, J.G., Kerver, J.K., Hafford, J.A., Osoba, J.S., 1952. Laboratory Determination of Relative Permeability. Journal of Petroleum Technology 4, 187–196. https://doi.org/10.2118/952187-G

Ringrose, P.S., Jensen, J.L., Sorbie, K.S., 1996. Use of Geology in the Interpretation of Core-Scale Relative Permeability Data. SPE Formation Evaluation 11, 171–176. https://doi.org/10.2118/28448-PA

Sandstone Cores at Kocurek Industries. [WWW Document], n.d. Sandstone Cores. URL https://kocurekindustries.com/sandstone-cores (accessed 9.22.18).

Scholle, P.A., 1999. Laminated sandstones and starved ripples in Cherry Canyon Formation [WWW Document]. URL https://geoinfo.nmt.edu/staff/scholle/graphics/permphotos/105.html

Welge, H.J., 1952. A Simplified Method for Computing Oil Recovery by Gas or Water Drive. Journal of Petroleum Technology 4, 91–98. https://doi.org/10.2118/124-G